Antarctic icebergs distributions 1992-2014

Jean Tournadre, Nicolas Bouhier, Fanny Girard-Ardhuin, F. Remy

AGU PUBLICATIONS

JGR

Journal of Geophysical Research: Oceans

RESEARCH ARTICLE

10.1002/2015JC011178

Antarctic icebergs distributions 1992–2014

J. Tournadre[1], N. Bouhier[1], F. Girard-Ardhuin[1], and F. Rémy[2]

[1]Laboratoire d'Océanographie Spatiale, IFREMER, Plouzané, France, [2]Laboratoire d'Etudes en Géophysique et Océanographie Spatiales, CNRS, Toulouse, France

Key Points:
- 1992–2014 small icebergs (<8 km^2) database and monthly ice volume climatology for the Southern Ocean
- Icebergs size distribution follows a −3/2 power law representative of brittle fragmentation
- Small icebergs are mainly generated by the fragmentation of larges ones

Supporting Information:
- Supporting Information S1

Correspondence to:
J. Tournadre,
jean.tournadre@ifremer.fr

Citation:
Tournadre, J., N. Bouhier, F. Girard-Ardhuin, and F. Rémy (2016), Antarctic icebergs distributions 1992–2014, *J. Geophys. Res. Oceans*, *121*, 327–349, doi:10.1002/2015JC011178.

Received 28 JUL 2015
Accepted 4 DEC 2015
Accepted article online 13 DEC 2015
Published online 11 JAN 2016

Abstract Basal melting of floating ice shelves and iceberg calving constitute the two almost equal paths of freshwater flux between the Antarctic ice cap and the Southern Ocean. The largest icebergs (>100 km^2) transport most of the ice volume but their basal melting is small compared to their breaking into smaller icebergs that constitute thus the major vector of freshwater. The archives of nine altimeters have been processed to create a database of small icebergs (<8 km^2) within open water containing the positions, sizes, and volumes spanning the 1992–2014 period. The intercalibrated monthly ice volumes from the different altimeters have been merged in a homogeneous 23 year climatology. The iceberg size distribution, covering the 0.1–10,000 km^2 range, estimated by combining small and large icebergs size measurements follows well a power law of slope -1.52 ± 0.32 close to the $-3/2$ laws observed and modeled for brittle fragmentation. The global volume of ice and its distribution between the ocean basins present a very strong interannual variability only partially explained by the number of large icebergs. Indeed, vast zones of the Southern Ocean free of large icebergs are largely populated by small iceberg drifting over thousands of kilometers. The correlation between the global small and large icebergs volumes shows that small icebergs are mainly generated by large ones breaking. Drifting and trapping by sea ice can transport small icebergs for long period and distances. Small icebergs act as an ice diffuse process along large icebergs trajectories while sea ice trapping acts as a buffer delaying melting.

1. Introduction

Snow that precipitates over the Antarctic ice sheet and transforms into ice ultimately returns as freshwater to the ocean, either along the coast as basal melting of the floating ice shelves or into the Southern Ocean as melting of drifting icebergs. Iceberg calving has long been assumed to be the dominant cause of mass loss for the Antarctic ice sheet. In 1992, using sparse shipborne data and satellite tracking from the U.S. National Ice Center (NIC), *Jacobs et al.* [1992] estimated the calving fluxes to be 2016 ± 672 Gt yr^{-1}. Their estimates, based on many assumptions about the volume, density, and lifetime of icebergs, have been widely used in physical oceanography studies, in particular numerical ocean circulation modeling of the Southern Ocean [*Gladstone et al.*, 2001; *Silva et al.*, 2006; *Stammer*, 2008; *Lellouche et al.*, 2013] as well as in studies on the impact of icebergs on transport of nutriment (labile iron) and primary production [*Raiswell et al.*, 2008; *Lancelot et al.*, 2009]. In the early 2000s, the importance of melting near the calving front has been demonstrated [*Rignot and Jacobs*, 2002; *Joughin and Padman*, 2003], but until recently, no study reliably quantified the calving flux and the basal mass balance for the whole of Antarctica. Fresh water enters the Southern Ocean following different paths: whereas basal meltwater is distributed over the upper few hundred meters of the coastal water column, icebergs drift and melt farther away from the continent. Having good constraints on these fluxes and their distribution can improve our understanding of Antarctic deepwater formation and of the hydrography of the Southern Ocean.

In 2013, two studies [*Rignot et al.*, 2013; *Depoorter et al.*, 2013] using both satellite data of calving and grounding-line fluxes and modeled ice-shelf snow accumulation rates estimated very similar basal meltwater productions of ice shelves of 1500 ± 237 and 1454 ± 174 Gt yr^{-1}, respectively, and calving fluxes of 1265 ± 141 and 1321 ± 44 Gt yr^{-1}. They gave thus an estimate of the distribution of fresh water in the Southern Ocean and its partitioning between the liquid and solid phases. Ice-shelf melting equals or exceeds the calving flux. Both studies also presented a distribution of the mean basal mass-loss rates of ice shelves around Antarctica that can be used for example to constrain numerical model.

Combining the NIC and Brigham Young University iceberg tracking databases and satellite altimetry data, *Tournadre et al*. [2015] calculated the volume of large icebergs (>18 km in length) and estimated the distribution of the volume of ice they transport as well as their calving flux during the 2002–2012 period at 960 ± 72 km^3 yr^{-1}. Depending on their size, and drift path, large icebergs can have extremely long lifetimes and thus act as a buffer for the transport of freshwater into the ocean. However, although they constitute the major part of the volume of ice, *Tournadre et al*. [2015] showed that their basal melting (∼18%) is small compared to their breaking into smaller icebergs that are not detected by NIC and BYU. Smaller icebergs (<18 km) act as a diffuse process for ice transport and are a major contributor to the transport of freshwater away from the Antarctic continent. The distributions of small icebergs and of the volume of ice they transport are thus key parameters to better understand the freshwater flux in the Southern Ocean. The transfer of ice from large to small icebergs through fragmentation, necessary for a better numerical modeling of the freshwater flux, could also be improved if the size distribution of icebergs from small (∼1 km^2) to large (>1000 km^2) were better estimated.

Tournadre et al. [2008] demonstrated that small icebergs (0.1–3 km in length) have a detectable signature in open sea (free of sea ice) in the noise part of high-resolution (HR) altimeter waveforms and they estimated a monthly small iceberg probability distribution by analyzing 1 year of Jason-1 altimeter waveforms. *Tournadre et al*. [2012] proposed a method to estimate, under assumptions on free-board height and ice backscatter, the iceberg area and thus the iceberg volume. Using the complete Jason-1 archive (from 2002 to 2010), they created a small iceberg data base for the Southern Ocean which gave the first description of small iceberg distribution in open water at unprecedented time and space resolutions. However, because of the low inclination of the Jason-1 satellite, primarily designed for ocean studies, the iceberg distribution was limited to the north of 66°S (up to 45°S), which hampers the analysis of the South Pacific and Atlantic Oceans.

Following these studies, the ALTIBERG project was funded by the French Centre National d'Etudes Spatiales (CNES) to create a small iceberg database using the high-resolution waveforms of all past and present altimeters covering the 1992 to present period. The present paper details the database (freely available at the CERSAT website http://cersat.ifremer.fr/data/products/catalogue, project altiberg) and presents a first analysis of the results.

Section 2 gives a general description of the database: altimeter data used in the study, method of detection, computation of the ice volume, and intercomparison and validation of the different altimeters estimates. The large iceberg databases also used in the study are briefly described in section 3. Section 4 presents a unified size distribution covering the 1–10,000 km^2 range. The spatiotemporal variability of the distribution of the small iceberg volume of ice and the relations between the volume of ice transported by small and large icebergs are analyzed in section 5.

2. The ALTIBERG Icebergs Database

Any target emerging from the sea surface has a detectable signature in the noise part (i.e., the portion of the echo waveform above the sea surface) of high-resolution satellite altimeter waveforms if its backscatter is large enough to come out of the thermal noise and if its range is within the altimeter range analysis window [*Tournadre*, 2007; *Tournadre et al*., 2008]. The signatures of icebergs in the waveform space (along-track position and range) are parabolas whose shape is determined by the satellite orbits parameters. The detection method, given in Appendix A, was first applied to the Jason-1 altimeter archive (2002–2012) to estimate the distribution of small icebergs (between 0.1 and 8 km^2) and the associated volume of ice in the Southern Ocean on a monthly basis [*Tournadre et al*., 2012]. It has been adapted in function of satellite orbit and sensors characteristics to process the archives of nine past and present satellite altimeter missions. The database of Southern Ocean icebergs created covers 23 years (1992–2014). The database contains the icebergs latitude, longitude, time, range, backscatter, and area and distance from nadir estimated from the inversion of range and backscatter (see Appendix B).

2.1. The Altimeter Missions

The nine altimeters used are the three NASA/CNES missions of the Topex/Jason series (Topex/Poseidon, Jason-1, and Jason-2), the three ESA ERS-Envisat missions (ERS-1, ERS-2, and Envisat), and three specific missions: the ESA's Cryosat dedicated to the study of the cryosphere, the CNES/ISRO SARAL/AltiKa whose altimeter operates at Ka band and the China National Space Administration (CNSA) Hai Yáng 2A (HY2A) ocean

Table 1. Main Characteristics of the Radar Altimeters Used to Build the Data Base

Altimeter	Time Period	Altitude (km)	Inclination (°)	Beam Width	Freq. (GHz)	Numbers of Bins	Track Point	Bin Width (ns)	Waveform Frequency (Hz)	Repeat Period (day)
ERS-1	1992–1996	784	98	1.3	Ku-13.8	64	32.5	3.03	∼20	3–35–168
ERS-2	1995–2003	784	98	1.3	Ku-13.8	64	32.5	3.03	∼20	35
Topex	1992–2005	1334	66	1.1	Ku-13.6	128	32.5	3.125	∼10	10
Jason-1	2002–2012	1334	66	1.3	Ku-13.6	104	32.5	3.125	∼20	10
Envisat	2002–2012	784	98	1.3	Ku-13.57	128	43	3.125	∼20	35
Jason-2	2008–	1334	66	1.3	Ku-13.5	104	32.5	3.125	∼20	10
Cryosat	2010–	717	90	1.2	Ku-13.57	128	34.5	3.125	∼20	∼30
ALTIKA	2013–	796	98.55	0.61	Ka-35.75	128	52	2.0	∼40	35
HY2A	2011–	963	99.35	0.91	Ku-13.58	128	32.5	3.125	∼20	14

satellite. The satellites' orbit and sensor characteristics are given in Table 1. The 66° inclination of the Topex-Jason satellites limits their coverage to latitudes lower than 66°S and thus their sampling of the southern Atlantic and Pacific Oceans. The Cryosat Synthetic Aperture Interferometric Radar Altimeter (SIRAL) provides three operational modes: Low-resolution (LRM) mode like a conventional altimeter, SAR mode operating a high-resolution measurement on sea ice, SAR interferometer (SARIn) mode operating on rough surfaces like on the sea ice/land limit.

The SAR mode, selected from a mask of geographical zones updated every 2 weeks to allow for changes in sea ice extent, includes the sea ice and a margin zone over the open ocean of some hundreds kilometers. At present, the detection is only performed on LRM data, which greatly limits the detection capability of Cryosat. In the future, a specific detection algorithm will be developed for the SAR mode in order to complement the database near sea ice.

All altimeters but Altika operate at Ku band and several altimeters have dual frequency capabilities (Topex and Jason-1). For them, the detection is conducted only on Ku band data. The waveform repetition frequency is in general around 20 Hz except for Topex (10 Hz) and Altika (40 Hz). The number of waveform bins varies from 64 for the older altimeters to 128 for the new ones. The nominal track point, corresponding to the sea surface, is in general set at 32.5 except for Envisat (43) and Altika (52). The noise part of the waveform ranges from bin 1 to the track point. Because of the effect of waves on the waveform leading edge, the noise level in the five to eight bins before the track point is too high for a good detection and those bins are thus not used. The first three to eight bins can also present a high noise level mainly because of spectral leakage during the onboard processing and cannot be used. For Altika, the first 13 bins are set to zero on board and are thus not considered. The bins used for detection are given in Table 2.

The noise level of the usable bins is a crucial parameter for the stability and quality of the detection. It has been monitored over the lifetime of the instruments and is remarkably stable for all altimeters except for Topex. Indeed, starting in 1996, the aging of the Topex altimeter degraded the performance of the sensor and lead to a strong increase of the noise level (see Figure 1) that also slowly degraded the performances of iceberg detection. In 1999, the switch to the backup Topex (side B) instrument was made necessary. From 1996 to 1999, the Topex noise level is too high for the data to be used for iceberg detection. As the characteristics of Topex A and B are sensibly different, they have been considered as two different altimeters. After March 2012 until its loss in June 2013, Jason-1 was placed on a geodetic orbit at 1324 km altitude with a repeat period of 406 days. Because of the change of sampling pattern, it is considered as a different mission in the database (Jason-1B).

Table 2. Detection Parameters for the Different Altimeters

Altimeter	Waveform Usable Bins	1 Hz σ_0 Calibration Versus Jason-1 (dB)	σ_0 Calibration 20 Hz	A_{SW} km^2
ERS-1	6-26	2.7	0.4	19.8
ERS-2	6-26	2.7	0.3	19.8
Topex	8-26	2.4	0.4 (A), 0.2 (B)	28.5
Jason-1	5-24	0	0	34.8
Envisat	7-39	2.9	0.3	41.2
Jason-2	3-24	0	−0.6	37.7
Cryosat	6-25	0.42	0	19.2
ALTIKA	14-45	2.5	−2.0	26.3
HY2A	2-24	1.86	−1.0	23.7

2.2. Intercomparison of Data Sets

To obtain a continuous and homogeneous 23 year time series using nine different instruments, the

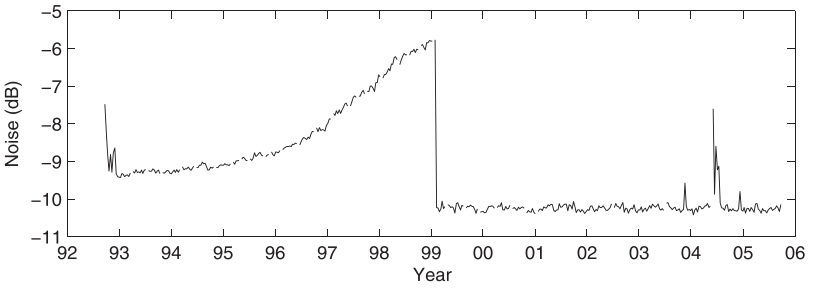

Figure 1. Mean noise of the usable bins of the Topex waveforms estimated for each 10 day cycle.

data have been intercalibrated. First, the backscatter coefficients of each altimeter, except Cryosat, HY2A, and Altika, were calibrated versus Jason-1 using the 1 Hz calibration coefficients of *Queffeulou* [2013] presented in Table 2. The Cryosat, HY2A, and Altika coefficients come from the calibration studies versus Jason-2 of *Scharroo et al*. [2012], *Raynal* [2014], and *Thibaut and Steunou* [2013], respectively. Figure 2 presents the nine probability density functions (pdf) of iceberg backscatter. The pdfs separate into two main groups corresponding to polar orbiting satellites (800–900 km orbits) and to the Topex-Jason series at 1300 km altitude. The pdfs are almost identical for Jason-1(B) and Jason-2 as well as for ERS-1 and ERS-2 whose sensors

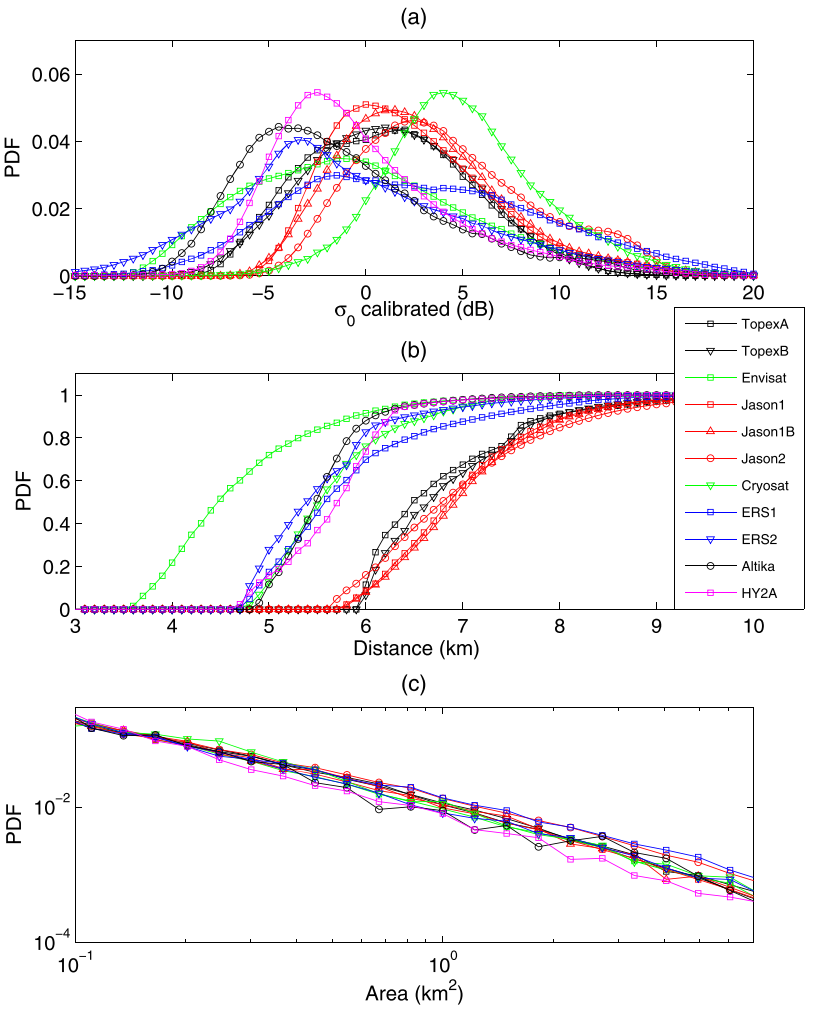

Figure 2. Probability density function of (a) icebergs backscatter, (b) cumulative density function of distance from nadir, and (c) probability density function of area.

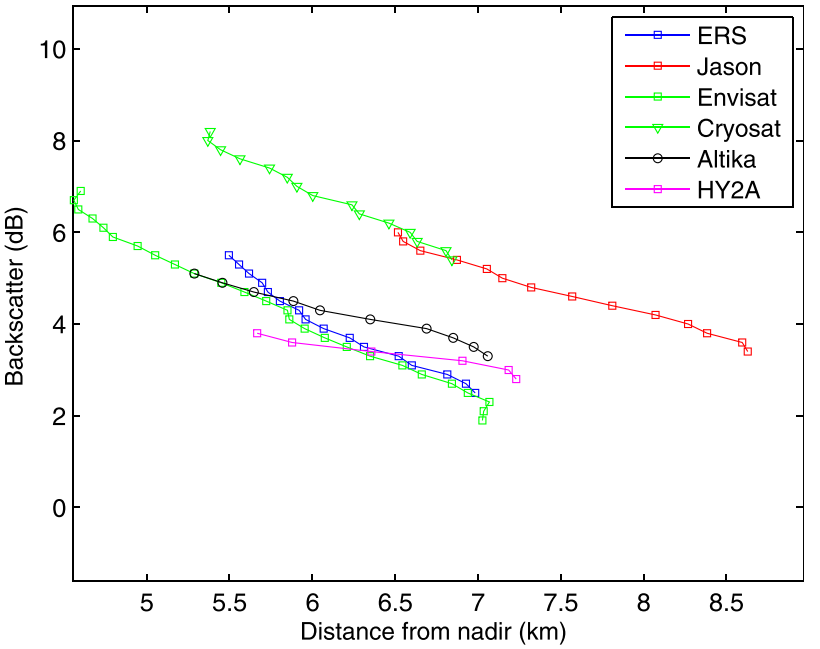

Figure 3. Modeled backscatter of a 1 km^2 iceberg as a function of distance from nadir for the different altimeter.

characteristics are almost identical. The shape of the pdf depends on the number of bins used for detection; a larger number corresponding to a larger range of backscatter. The differences of pdfs also result from the difference of backscatter from a given iceberg depending on the satellite and sensor characteristics as shown in Figure 3 which presents the backscatter of a 1 km^2 iceberg as a function of distance from nadir from the model functions (see Appendix B) used to infer iceberg area from range and backscatter. The backscatter for Topex/Jason and Cryosat satellites is about 2 dB larger than that for other ones. A second backscatter calibration was also estimated by adjusting the pdf of area versus Jason-1. These corrections, also given in Table 2, are significant only for HY2A and Jason-2. Altika correction takes into account the backscatter difference over ice between Ka and Ku bands estimated by *Rémy et al.* [2015].

The cumulative distributions of distance from nadir presented in Figure 2b also clearly separate into two main groups corresponding to satellite altitude. The distribution's width depends on the number of bins used for detection and on the bin width (see Appendix C). It is maximal for Envisat. The surface normalization coefficients, estimated using equation (C4), used to compute the volume of ice are given in Table 2.

The distributions of iceberg area, presented in Figure 2c, show the very good agreement between the different altimeters. Each distribution has been fitted by lognormal and power law distributions (see Appendix D). Only area larger than 0.1 km^2 have been considered to limit the effect of the differences of sensor's sensitivity for very small icebergs. The parameters of the fitted laws are given in Table 3 as well as the number of detected icebergs. The power law slopes vary from −1.23 to −1.49 with a mean value of −1.39 while the μ and σ parameters of the lognormal laws vary from −0.86 to −1.75 and 1.66 to 2.08, respectively with means of −1.18 and 1.84. Considering the large differences in the number of detected icebergs, which varies by more than a factor 10, and the natural variability of icebergs during the different period of operation of the nine missions, the distributions are in good agreement and can be considered as representing a homogeneous population.

Table 3. Analysis of the Icebergs Area Distributions: Parameters of Fitted Lognormal and Power Laws Distributions

	Number of Iceberg	Lognormal		Power Law Slope
		μ	σ	
ERS-1	7,683	−0.95	2.08	−1.23 ± 0.02
ERS-2	18,424	−1.28	1.95	−1.36 ± 0.02
Topex A	4,508	−1.12	1.79	−1.42 ± 0.02
Topex B	28,208	−1.11	1.74	−1.43 ± 0.03
Jason-1	60,471	−1.18	1.79	−1.41 ± 0.02
Jason-1B	3,050	−1.11	1.74	−1.43 ± 0.04
Envisat	52,729	−1.31	1.89	−1.39 ± 0.01
Jason-2	22,156	−0.86	1.88	−1.28 ± 0.02
Cryosat	3,310	−1.03	1.66	−1.44 ± 0.02
ALTIKA	2,907	−1.34	2.00	−1.35 ± 0.05
HY2A	19,366	−1.75	1.68	−1.49 ± 0.02

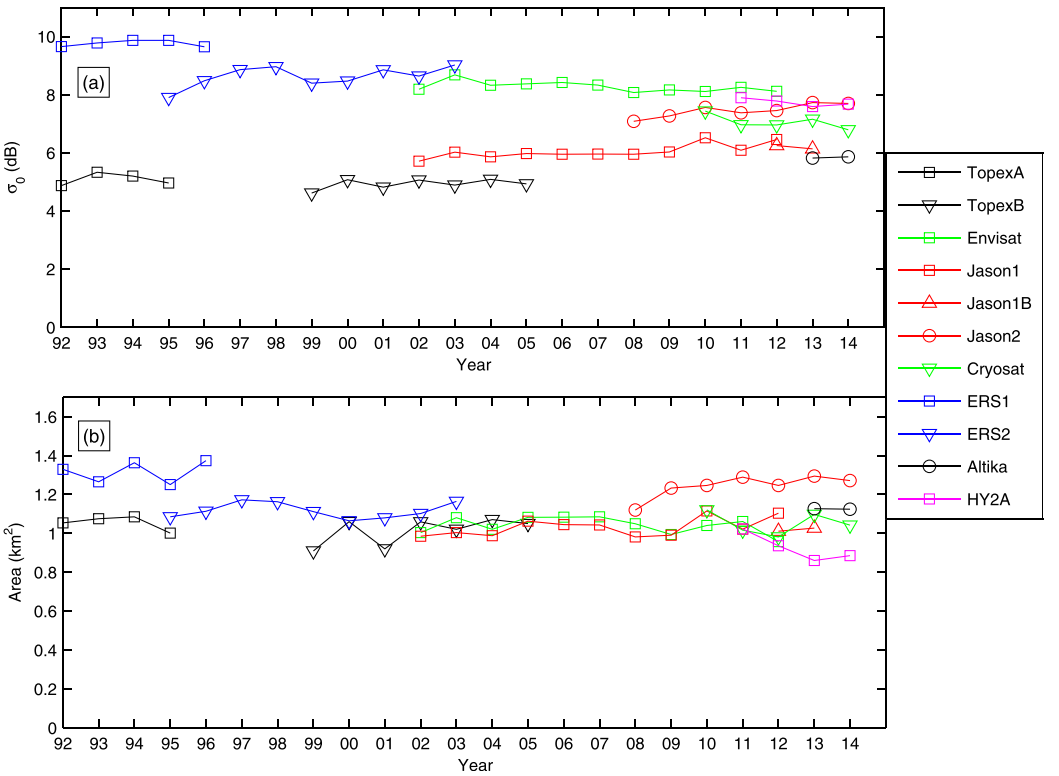

Figure 4. Evolution of the (a) mean annual backscatter and (b) area.

The data sets homogeneity and the detection stability were further ensured by monitoring the variability of the mean annual backscatter and area (presented in Figure 4). Over the missions' lifetime, backscatter varies by less than 1 dB while the area by less than 0.2 km^2. No significant drifts over time were detected for both parameters.

2.3. Volume of Ice

2.3.1. Volume of Ice by Altimeter

The monthly volume of ice in open sea was computed for each altimeter over a regular 100 km resolution polar grid using the method presented by *Tournadre et al*. [2012] and detailed in Appendix C. For some months, the volume of ice cannot be estimated because of the degrading of the sensor (TopexA) or of the loss of data (ERS-2, early 2001). The monthly total volume of ice and the volume North of 66°S, for a better intercomparison with the Topex/Jason series, are presented in Figure 5. The mean difference of monthly total volume of ice from the different altimeters during their common time of operation is presented in Table 4. For missions with similar sampling and sensor characteristics such as Jason-1 and Jason-2 or ERS-2 and Envisat, the mean difference is less than 5 km^3/month. For other missions, it is between 3.3 and 21.5 km^3/month. The maximum of 21.5 km^3 between HY2A and Jason-2 represents 19.6% of the mean monthly volume. This is smaller than the 26% uncertainty on ice volume estimated by *Tournadre et al*. [2012] from Jason-1 data. Some large differences of monthly volume can be seen in Figure 5 in early 2000 or in 2004. They all involve Topex and can be related to the fact that it provides significantly less data because of its lower waveform repetition frequency (10 Hz) and of its time-sharing mode of operation with the Poseidon altimeter (not processed) which operates 10% of the time. This leads to a higher uncertainty on volume estimate. However, the overall intercomparison of volume estimates shows, considering the sampling and sensor characteristic differences of the nine missions, an agreement good enough to allow the merging of the different volume estimates.

2.3.2. Merging the Different Altimeters

The nine volume estimates were merged to produce a homogeneous time series covering the 1992–2014 period. The merged product is obtained by a weighted sum of the individual products, i.e.,

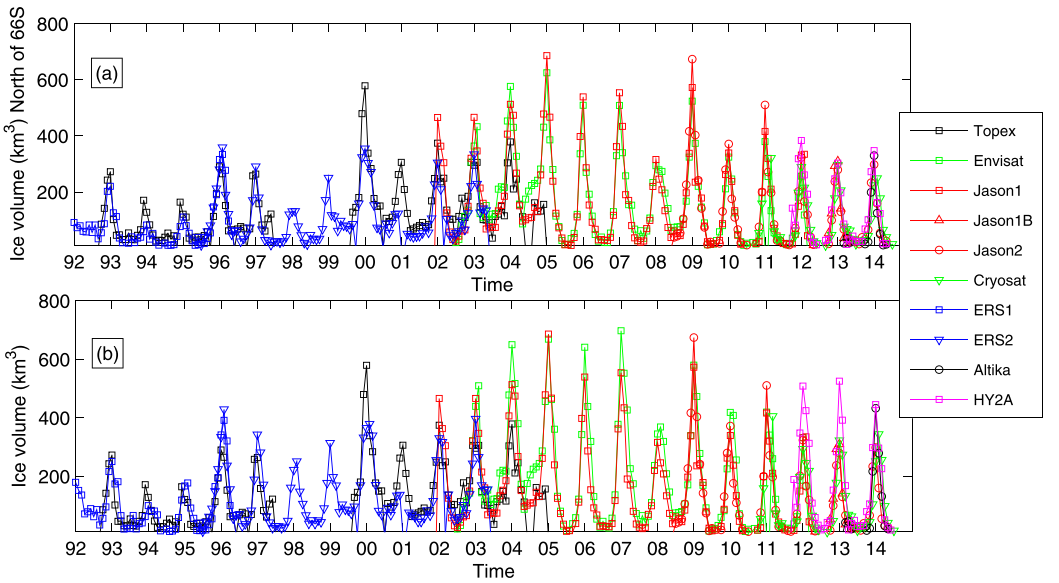

Figure 5. Monthly total volume of ice in open sea from each altimeter on a regular 100 × 100 km^2 polar grid (a) North of 66°S and (b) for the entire Southern Ocean.

$$V_m(i,j,t) = \sum_{l=1}^{n} V_l(i,j,t) * w_l \tag{1}$$

where the weights w_l are given by

$$w_l = \frac{N_S^l(i,j,t)_i}{\sum_{k=1}^{n} N_S^k(i,j,t)} \tag{2}$$

where N_S^l is the number of valid data for satellite l and n is the number of available satellites.

3. Large Iceberg Databases

The NIC Southern Hemisphere Iceberg database (available at http://www.natice.noaa.gov) contains the position and size (length and width) estimated by analysis of visible or SAR images of icebergs larger than 10 nautical miles (18.5 km) along at least one axis. It is updated weekly. Every iceberg is tracked, and when imagery is available, information is updated and posted. The NIC assigns each iceberg a name composed of a letter indicating its point of origin and a running number. The letters used are as follows: A, longitude 0°–90°W (Bellingshausen Sea and Weddell Sea); B, longitude 90°W–180° (Amundsen Sea and Eastern Ross Sea); C, longitude 90°E–180° (Western Ross Sea and Wilkes Land); and D, longitude 0°–90°E (Amery Ice Shelf and Eastern Weddell Sea).

Table 4. Intercomparison of the Monthly Total Volume (in km^3/Month) of Ice in Open Sea From the Different Altimeters During Their Overlapping Operation Time

	Topex	ERS-1	ERS-2	Envisat	Jason-1	Jason-1B	Jason-2	Cryosat	Altika
ERS-1	6.3								
ERS-2	16.6	17.6							
Envisat	14.6		0.7						
Jason-1	4.0		2.4	11.0					
Jason-1B									
Jason-2				7.1	4.8	12.9			
Cryosat				1.5	20.6	14.5	10.2		
Altika							8.9	3.3	
HY2A						4.1	21.5	6.9	14.5

The BYU Center for Remote Sensing maintains an Antarctic Iceberg Tracking Database (http://www.scp.byu.edu/data/iceberg/database1.html) for icebergs larger than 6 km in length [*Stuart and Long*, 2011]. Using six different satellite scatterometer instruments, they produce since 1992 a track database that includes icebergs identified in enhanced resolution scatterometer backscatter images. The initial position for each iceberg is located based on a position reported by NIC or by the sighting of a moving iceberg in a time series of scatterometer images. The iceberg name is the NIC one except for those detected in scatterometer data only that are named UK (for "unknown"). Figure 9c presents all the iceberg locations between 1 January 1992 and 31 December 2012 used in this study.

The database of volume of large icebergs compiled by *Tournadre et al*. [2015] covers the 2002–2012. It is based on the combined analysis of the NIC/BYU icebergs trajectories and the archive of Jason-1, Jason-2, and Envisat waveform altimeters. It contains the daily position, mean free-board, length, width, area, and volume of the NIC/BYU icebergs. For the 2002–2012 period, among the 309 identified icebergs, 113 are common to NIC and BYU databases and 196 are "unknown."

4. Unified Iceberg Size Distribution

Several studies have been published presenting the size distribution of small Antarctic icebergs (length smaller than some kilometers) using ship observations [*Jacka and Giles*, 2007; *Romanov et al*., 2008, 2012] and satellite altimetry [*Tournadre et al*., 2012]. Recently, *Tournadre et al*. [2015], combining altimetry and the NIC and BYU data bases, presented a size distribution for icebergs larger than 10 km in length. However, very few studies proposed a size distribution covering the whole range of iceberg size. Using a limited data set of SAR images from the Radarsat-1 Antarctic Mapping Project (RAMP) that are snapshots taken from September to October 1997 and are restricted to the near-coastal zone, *Wesche and Dierking* [2015] detected 6912 icebergs larger than 0.3 km^2. They estimated a size distribution by surface area ranges with 71.9% of icebergs from 0.3 to 1 km^2, 26.0% 1–10 km^2, 1.8% 10–100 km^2, 0.2% 100–1000 km^2, and 0.1% 1000–10,000 km^2.

Combining the ALTIBERG small iceberg data base with the *Tournadre et al*. [2015], large iceberg ones provides a new opportunity to estimate a general size distribution. As different sensors and methods are used to infer the size of small and large icebergs, a unified distribution cannot be estimated by simple compilation of size estimates. It is built in the following way. The probability density function (pdf) of the size of icebergs larger than 200 km^2 is estimated using the large icebergs database for the 2002–2012 period. The 200 km^2 limit corresponds to the minimum iceberg size that is systematically detected by NIC. This pdf is then multiplied by the mean number of icebergs during the period to obtain the large iceberg size occurrence. The pdf of small icebergs size is estimated from the small iceberg database for the same period and the pdf is multiplied by the mean number of small icebergs for the months of January and February that corresponds to the minimum extent of sea ice and thus to the maximum number of icebergs to obtain the occurrence of small icebergs. The two distributions are then combined to obtain a global distributions that has no data in the 8–200 km^2 range. Figure 6 presents these experimental distributions. Both the small and large iceberg distributions follows well power laws of slope -1.41 ± 0.10 and -1.51 ± 0.95, respectively. The two distributions are quite remarkably aligned and present very similar slopes. It can thus be reasonably assumed that the global distribution also follows a power law, i.e., that there is a scale invariance of fracture and fragmentation processes in icebergs. The slope of the global fitted law is -1.52 ± 0.32. This slope is very close to $-3/2$ that has been shown both experimentally and theoretically to be representative of brittle fragmentation [*Astrom*, 2006; *Spahn et al*., 2014].

The -1.52 power law approximation gives a size distribution by range of 77% for icebergs <1 km^2, 17% for 1–10 km^2, 4.8% for 10–100 km^2, 1.5% for 100–1000 km^2, and 0.4% for 1000–10,000 km^2 (see Figure 6). This distribution agrees relatively well to the *Wesche and Dierking* [2015] one. However, it has less icebergs in the 1–10 km^2 range and more icebergs larger than 10 km^2. The RAMP data set is limited to coastal zones and does not cover the open ocean where most of the small icebergs are located leading to an underestimation of small icebergs while the number of large icebergs (NIC ones) significantly increased between 1997 (the RAMP period) and 2002 as already reported by *Long et al*. [2002] leading to a underestimation of the number of large icebergs. The power law can also be used to estimate the contribution of the different range of icebergs to the total surface, i.e., 0.9% <0.1 km^2, 2.5% 1–10 km^2, 7.4% 10–100 km^2, 22.2% 100–1000 km^2,

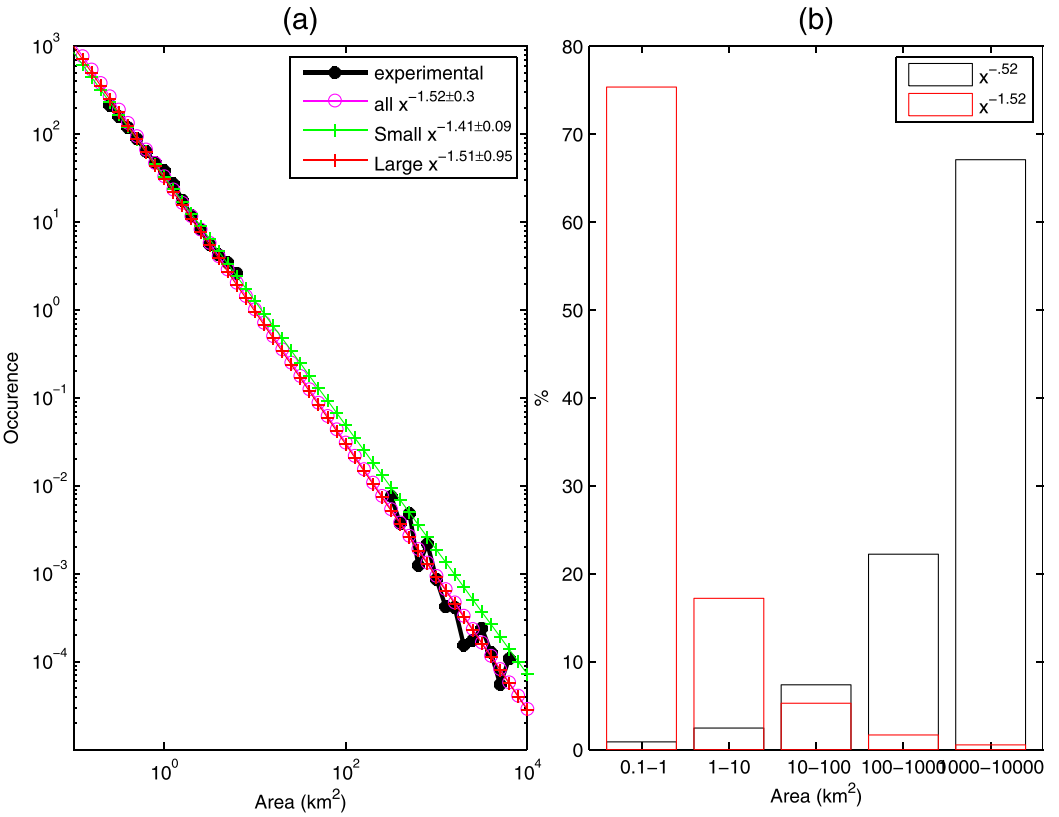

Figure 6. (a) Experimental size distribution (black line) and fitted power laws (small red line, large magenta line, and all green line) and (b) percentage of the total number of icebergs (red line) and of the total surface (black).

and 67.1% 1000–10,000 km^2. Assuming in a very crude first-order approximation that all icebergs have the same free-board, this distribution gives an idea of the general ice volume partition as a function of size and shows that large icebergs are the main vector of ice transport.

5. Analysis and Discussion

5.1. Temporal Variability: Impact of Sea Ice

The monthly volumes of ice are presented in Figure 8 as well as the volume in the three ocean basins: South Atlantic (SA) (70°W–30°E), South Indian (SI) (30°E–150°E), and South Pacific (SP) (150°E–70°W). The detection of small icebergs by altimeter being limited to open sea, the sea ice extent strongly conditioned the number of icebergs that can be detected and thus the volume of ice. The strong apparent seasonal cycle of volume primarily reflects the sea ice extent one, with maximums and minimums during the austral summer and winter, respectively. The times series of sea ice extent and volume in the Southern Ocean and in the three ocean basins are presented in supporting information Figure S1. Their correlation is −0.66 for the Southern Ocean showing a medium anticorrelation. It is only −0.45 for the Southern Indian. Figure 7 that presents the monthly anomalies of sea ice extent and volume clearly shows no direct correlation between the two series for all basins. The maximum correlation is only 0.16 for the Southern Indian and almost nil for the Southern Ocean and SP. Furthermore, the cross-correlation analysis of the anomalies presented in supporting information Figure S2 does not show any significant correlation for time lags less than 12 months.

As a consequence, it can be estimated that the large interannual variability of volume observed in the time series does not result from the interannual variability of the sea ice extent. The monthly summer maximum for each year presented in Figure 8b can be considered in a first-order approximation as the total volume of ice available during 1 year. It increases from about 150 km^3 in the 1990s to 750 km^3 in 2004 then decreases to 420 km^3 in 2014 in what can appear as an apparent 10 year cycle. The winter minimums are in general almost negligible but reached 130 km^3 in 2004. The large volume of ice observed in the different basins for

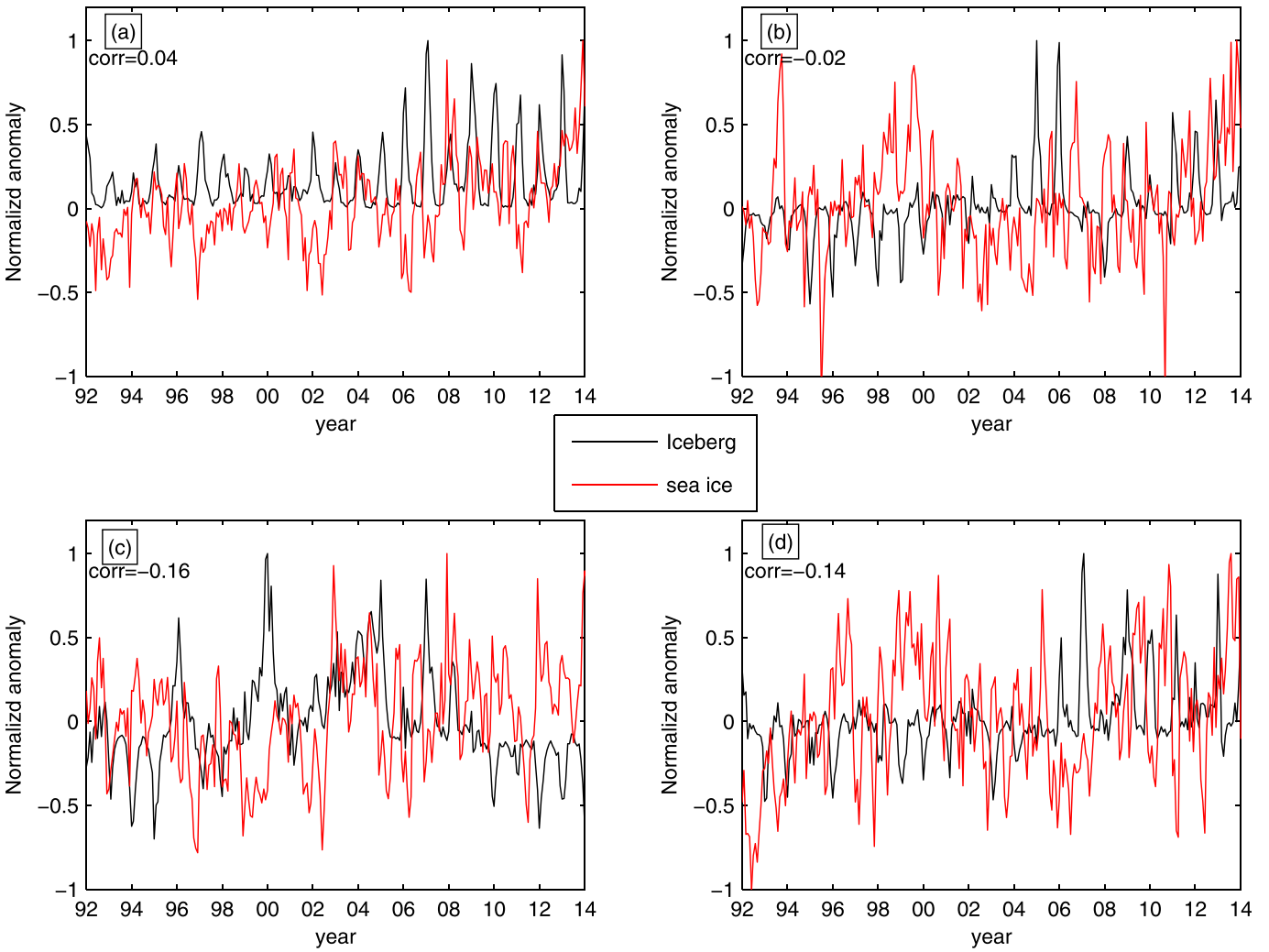

Figure 7. Normalized monthly anomalies of the sea ice extent and volume of small iceberg in open sea for the (a) Southern Ocean, (b) Southern Atlantic, (c) Southern Indian, and (d) Southern Pacific.

some years can sometimes be clearly associated with the northward drift and fragmentation of very large icebergs; for example: in SA, A22B, and B10A in 2000 and A32A in 1996, in SP C19A and B15A in 2007–2009, in SI, C20 in 2005–2006.

The Southern Ocean interannual variability and the three ocean basins ones are not in phase and years of global maximums can correspond to local minimums for a given basin like 2007 for SA or 2010 for SI. The distribution patterns can also significantly change from year to year. It can be easily seen in the mean annual distribution for the 23 years presented in supporting information Figures S3 and S4.

Over the 23 year period, SA is the main region of freshwater input into the ocean and represents 42% of the total volume of ice while SI and SP represent 22% and 35%, respectively. However, although SA is largely preponderant before 2004 with more than 50% of total ice, its contribution constantly decreases after 2004 to less than 30% after 2008 while SP accounts for about 50% after 2009 from 30 to 40% before.

The overall volume variability at least partially reflects the variability of the number of large icebergs as detected by NIC and BYU. The increase of volume between 1992 and 2004 is clearly associated with the large increase of the number of large icebergs already reported by *Long et al.* [2002]. Similarly, the decrease of the volume in SA after 2004 corresponds to a decrease of the large icebergs number in this basin. But the increase of large icebergs in SI after 2004 does not result in a significant increase of volume in SI. The

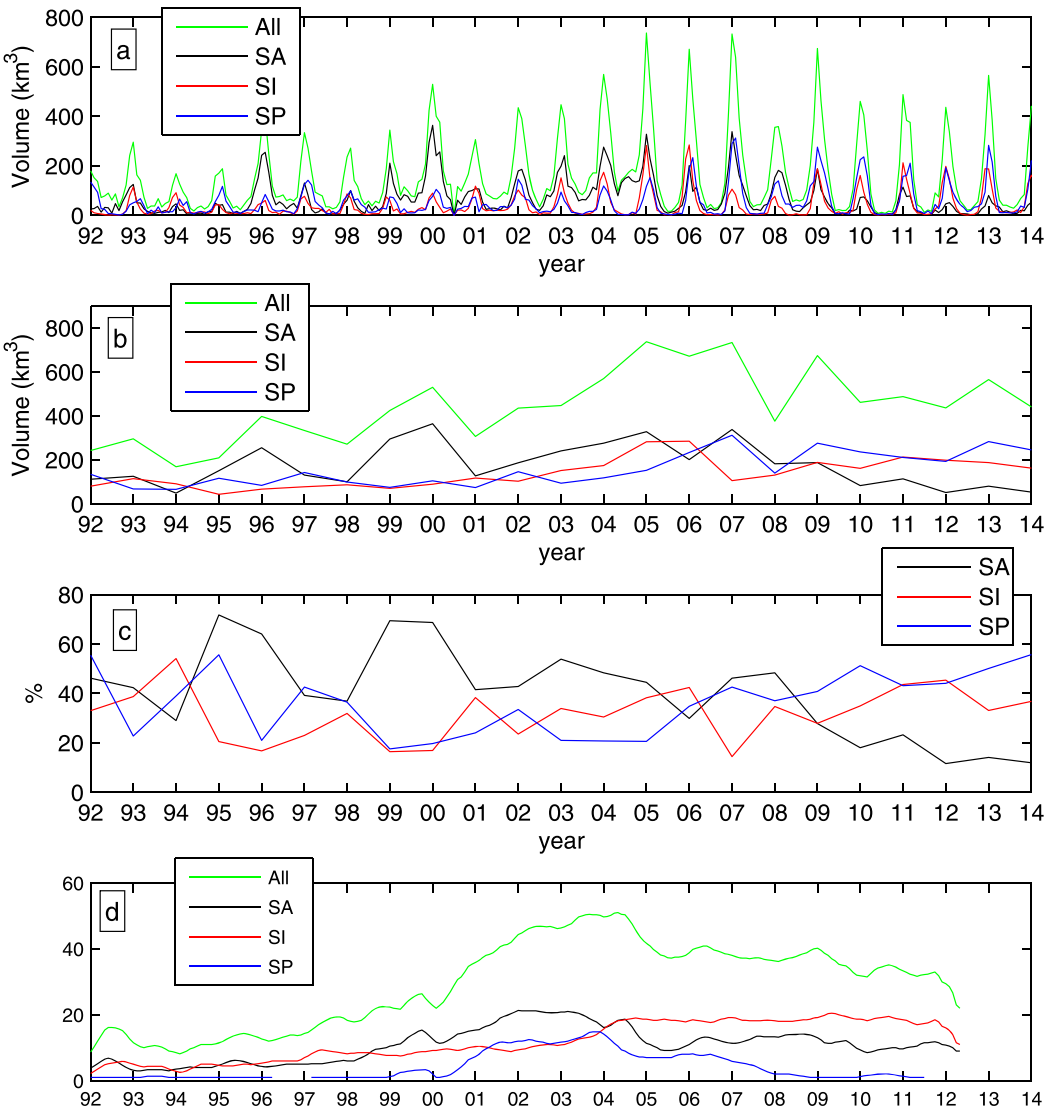

Figure 8. (a) Monthly total volume of ice in open sea by ocean basins, (b) maximum yearly volume of ice in open sea, (c) proportion of total volume by ocean basins, and (d) number of large NIC/BYU icebergs.

number of large icebergs cannot in itself explain all the small icebergs volume variability and the volume of ice of these large icebergs has to be considered.

5.2. General Patterns of the Distribution of Ice

The 12 year average monthly volume of ice presented by *Tournadre et al.* [2012] was based on the analysis of the Jason-1 archive alone and was thus limited to the north of 66°S. The new 23 year average of the summer (January–March) volume of small icebergs (<8 km^2) in open sea, presented in Figure 9, besides having a better statistical significance, allows a complete characterization of the ice distribution. The average volume for the four seasons is given in supporting information Figure S5. The grid points for which there is more than 11 months of sea ice per year in average during the 1992–2014 period are not considered. The distribution presents the three characteristic regions of maximum concentration, one in each ocean corresponding to the three main gyres (Ross, Weddell, and Kerguelen) of the general Southern Ocean circulation [*Orsi et al.*, 1995; *Jacobs et al.*, 2002; *McCartney and Donohue*, 2007; *Gladstone et al.*, 2001]. The maximum concentration is found in the Southern Atlantic Ocean (SA), in what has been called the "Iceberg Alley," and in the Southern Indian Ocean (SI) where it can exceed 1 km^3/month. In tSA, the region of concentration larger than 0.5 km^3/month extends from Graham Land (~60°W) to the west to almost 10°W to

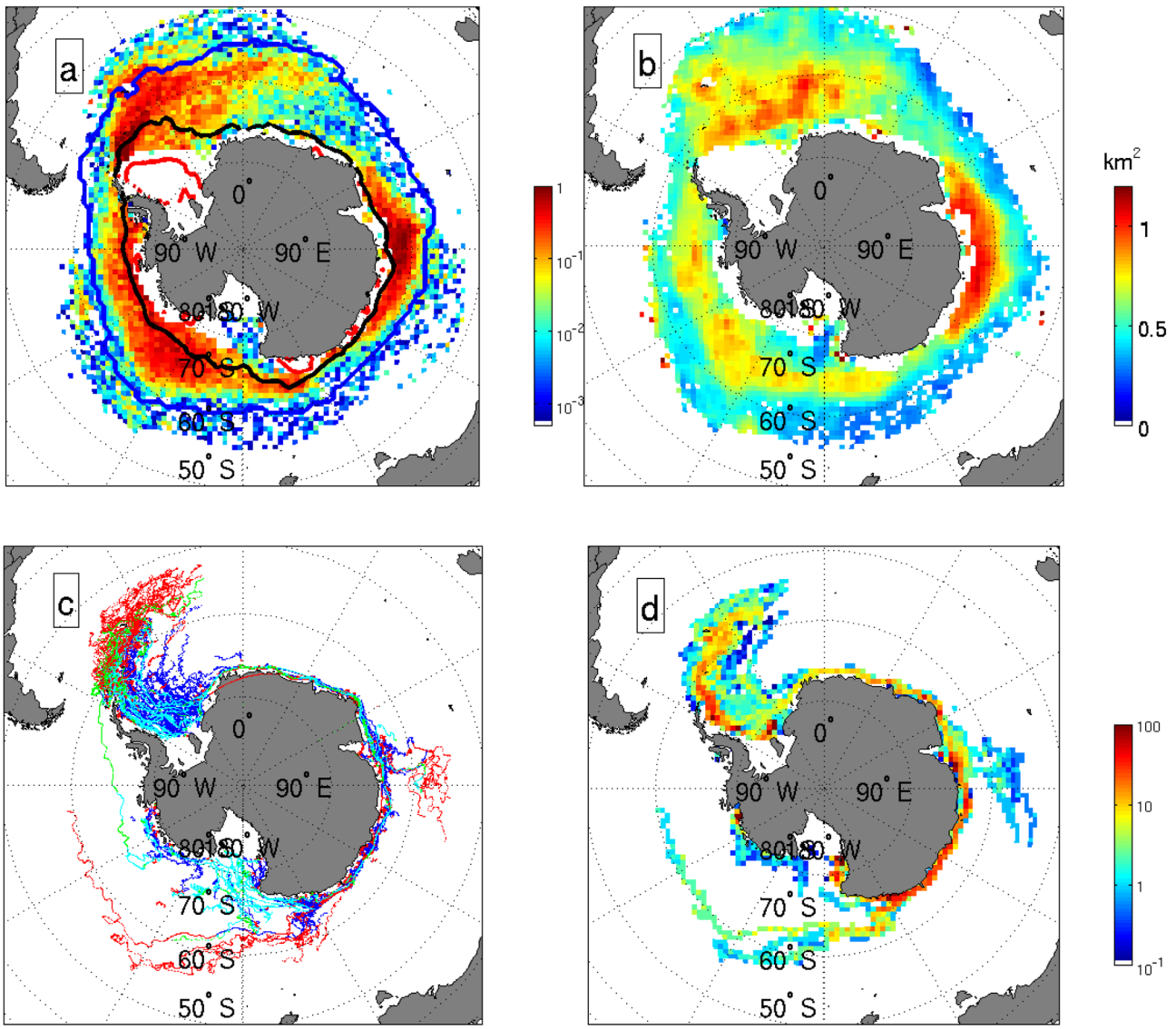

Figure 9. (a) Mean monthly volume (in km^3 per month per grid cell of 100×100 km^2) of small icebergs in open sea from 1992 to 2014 (the black, red lines indicate the mean maximum and minimum summer sea ice extent for the period from the SSM-I sea ice concentration data and the blue line indicates the mean annual maximum sea ice extent), (b) mean iceberg area 1992–2014, (c) trajectories of large icebergs from 1992 to 2012 from the NIC and BYU databases (trajectories within sea ice after 2002, blue lines; in open sea after 2002, red lines; within sea ice before 2002, light blue lines; and in open sea before 2002, green lines), (d) mean monthly volume (in km^3 per month per grid cell of 100×100 km^2) of large icebergs from 2002 to 2012. Figures 9a, 9b, and 9d fields are computed on a 100 × 100 km^2 polar grid.

the east. A secondary maximum zone of lower concentration (>0.1 km^3/month) extends along 58–59°S up to 10°E. This pattern shows the importance of the recirculation of icebergs within the eastern branch of the Weddell gyre along the Antarctic continent [*Klatt et al*., 2005]. Between 40°W and 30°E, the zone of high concentration extends much further north than the maximum sea ice extent and reaches 50°S. A weak relative maximum near 25–30°W confirms the observations of *Schodlok et al*. [2006] that the general iceberg drift in the Weddell Sea presents two distinctive patterns one to the west of 40°W where the icebergs drift close to the Antarctic Peninsula and a second weaker one, east of 40°W, corresponding to icebergs drifting in the Central and Eastern Weddell Sea.

The SI maximum, described in previous studies based on shipborne observations [*Jacka and Giles*, 2007; *Romanov et al*., 2008], extends from the Enderby land to the west (~60°E) to the Mertz Glacier to the east (~145°E). The maximum concentration is found between 60°E and 120°E and results from the calving from Amery, Shackleton, and West Ice shelves and from the westward drifts of the icebergs in the coastal current

[*Romanov et al*., 2008]. The icebergs remain confined along the continent except between 85°E and 115°E where the distribution extends north to 60°S as a result of the ocean circulation over the Kerguelen Plateau. The distribution is precise enough to allow the detection of small local maximums near emissary glaciers such as Mertz (144°E) and Ninnis (147°E) or near the Cook Ice shelf (150°E).

In the Southern Pacific (SP) Ocean, the volume maximum is lower than that in SI and SA at ∼0.5 km^3 and extends from 180°W to 90°W. The eastern limit is much further east into the Bellinghausen Sea than the typical 130°W eastern limit of the Ross gyre [*Riffenburgh*, 2007] and might reflect the presence of gyres in the Amundsen and Bellinghausen Seas indicated by models studies [*Grotov et al*., 1998]. The local maximum present near the Balleny islands (163°E) corresponds to icebergs drifting along the Victoria Land coast, exiting the Ross Sea around Cap Adare and turning eastward [*Keys and Fowler*, 1989; *Glasby*, 1990]. Calving from the Pine Island (100°W) and Land (142°W) glaciers, and from the Nickerson (145°W) and Wilkins (∼72°W) ice shelves, although of limited extent, is clearly visible. The iceberg concentration north of the maximum annual sea ice extent in SI and SP is low but still significant and corresponds to northward excursions of large icebergs caught in the Antarctic Circumpolar Current.

Figure 9c, which presents the NIC/BYU iceberg tracks from 1992 to 2013, clearly shows that small icebergs cover much larger regions of the Southern Ocean than large ones. Vast regions free of large icebergs, such as the North-Eastern Weddell Sea or the Bellinghausen Sea, contain significant amounts of ice, sometimes as high as 0.5 km^3/month, transported by small ones.

The mean iceberg area (see Figure 9b) decreases with decreasing latitude reflecting the melting and deterioration of icebergs during their northward travel into warmer waters. The largest ones are observed in SI Ocean near the Shackleton (60°W) and Amery (70°W) ice shelves, most probably because these calving zones are the northernmost leading to a more rapid retrapping of icebergs by sea ice, which increase their lifetime by limiting their open water travel and their deterioration. The size of the ice shelves located in this region may also influence the size of the icebergs although we lack of measurements to ascertain this fact. In SP, the mean area is significantly smaller than that in the two other basins, indicating that icebergs travel over larger distances and/or longer period in warmer water. In the SP and SI, some regions north of the maximum sea extent (around 60°S) are characterized by icebergs of quite large mean area that correspond to fragmentation of large icebergs drifting north.

6. Small-Large Icebergs Relations

Although small icebergs can calve directly from Antarctic ice shelves or glaciers, the major part results from the dislocation and breaking of large icebergs and many examples of this process can be found in satellite visible or SAR images. The Antarctic total calving flux has been estimated *Rignot et al*. [2013] and *Depoorter et al*. [2013] at 1265 ± 141 and 1321 ± 44 Gt yr^{-1}, respectively. *Tournadre et al*. [2015] using the NIC and BYU data base and altimeter data estimated the calving flux by icebergs larger than 200 km^2 at 960 ± 72 km^3 yr^{-1} (thus 850 Gt yr^{-1} assuming a 0.89 g/cm^3 ice density). Although the periods of analysis of these studies are different they can be used to estimate the order of magnitude of the calving of icebergs smaller than 200 km^2 should be of the order of 450 Gt yr^{-1}. Using the distribution of volume per iceberg size range presented in section 4, icebergs smaller than 8 km^2 represent less than 25% of this volume, i.e., 112.5 Gt yr^{-1}. This value is, except for some years, significantly smaller than the summer maximum (200–700 Gt) estimated by the altimeters. Fragmentation of large icebergs is most probably the main mechanism of generation of small icebergs. After their calving from large ones, small icebergs can either drift in open sea and melt or be trapped in sea ice and later released losing their direct connection with their "parents."

6.1. Distance Between Small and Large Icebergs

The distance between small icebergs and the nearest contemporary NIC/BYU large iceberg is used as a proxy to estimate the distance over which small icebergs traveled away from their source of origin. The geographical distribution of the proportion of small icebergs further than 500 km (median value of the distance) from large ones, presented in Figure 10, reveals two main regimes. The first one found in the Scotia Sea (between the Antarctic Peninsula and the South Georgia Island), along the Antarctic coast in the SI ocean, and in the Amundsen Sea, is characterized by a proximity between small and large icebergs, indicating that in these areas small icebergs calved either from large ones or from the same regions of Antarctica,

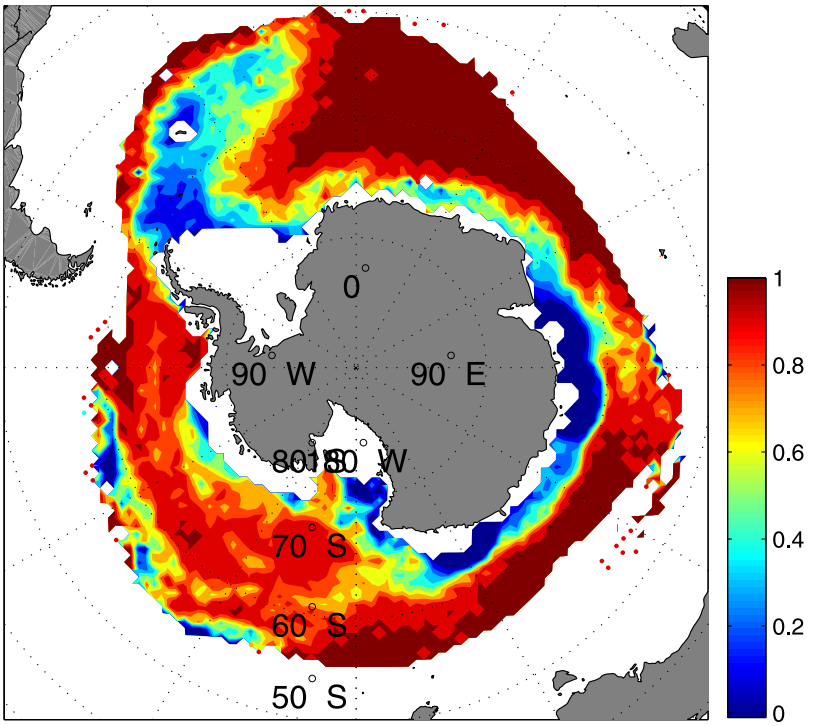

Figure 10. Proportion of icebergs distant by more than 500 km from a contemporary large one.

and/or drift along similar paths. This proximity is particularly clear in SP along 57°S where small icebergs result from the fragmentation of two large icebergs, C19A and B15A, that traveled north in 2008–2010.

The second regime corresponds to "free drifting" small icebergs that cannot be directly associated with a large one. Over vast zones of the Southern Ocean like the Ross, Bellinghausen, or Eastern Weddell Seas, the transport of ice and thus the freshwater flux result almost exclusively from small iceberg drifting over large distance, sometimes thousands of kilometers, from their calving sources, ice shelves, or most probably large icebergs.

The total volume of ice and the volumes for "close" and "free drifting" icebergs in the Southern Ocean and in the three basins are presented in Figure 11. The plots show the chaotic nature of ice distribution and the decorrelation between the total volume and its partition between the three basins. Over the whole period, 59% of the total volume (35% SA, 61% SI, and 78% SP) is transported by "free drifting" icebergs, which shows their importance to estimate the freshwater flux in the Ocean. However, before 1998 when the number of large icebergs is low, they represent more than 65% of the volume, but for most of the 2000s, this proportion drops to below 50%. The situation is more contrasted when considering the ocean basins. In SA, large icebergs frequently drift northward and free drifting icebergs represent only 35% of the volume but more than 50% before 2001 when the number of large icebergs is low and about 20% after. In SI, free drifting icebergs represent more than 70% of volume before 1999 and in 2010–2011 and about 35% between 2000 and 2010. In SP, the proportion is about 80–90% 1997–1998 and 2008–2009 when large icebergs drift north.

6.2. Relation Volume of Ice

The distance analysis gives only an insight into the relative positions of large and small icebergs but not into the transfer of ice from large to small icebergs. A simple method to analyze the relation between the volume of small and large icebergs is a correlation analysis. Figure 12 presents the normalized time series of small and large icebergs volumes for the Southern Ocean and the three basins during the 2002–2012 period. Only the large icebergs present in open water have been considered for a better comparison. The

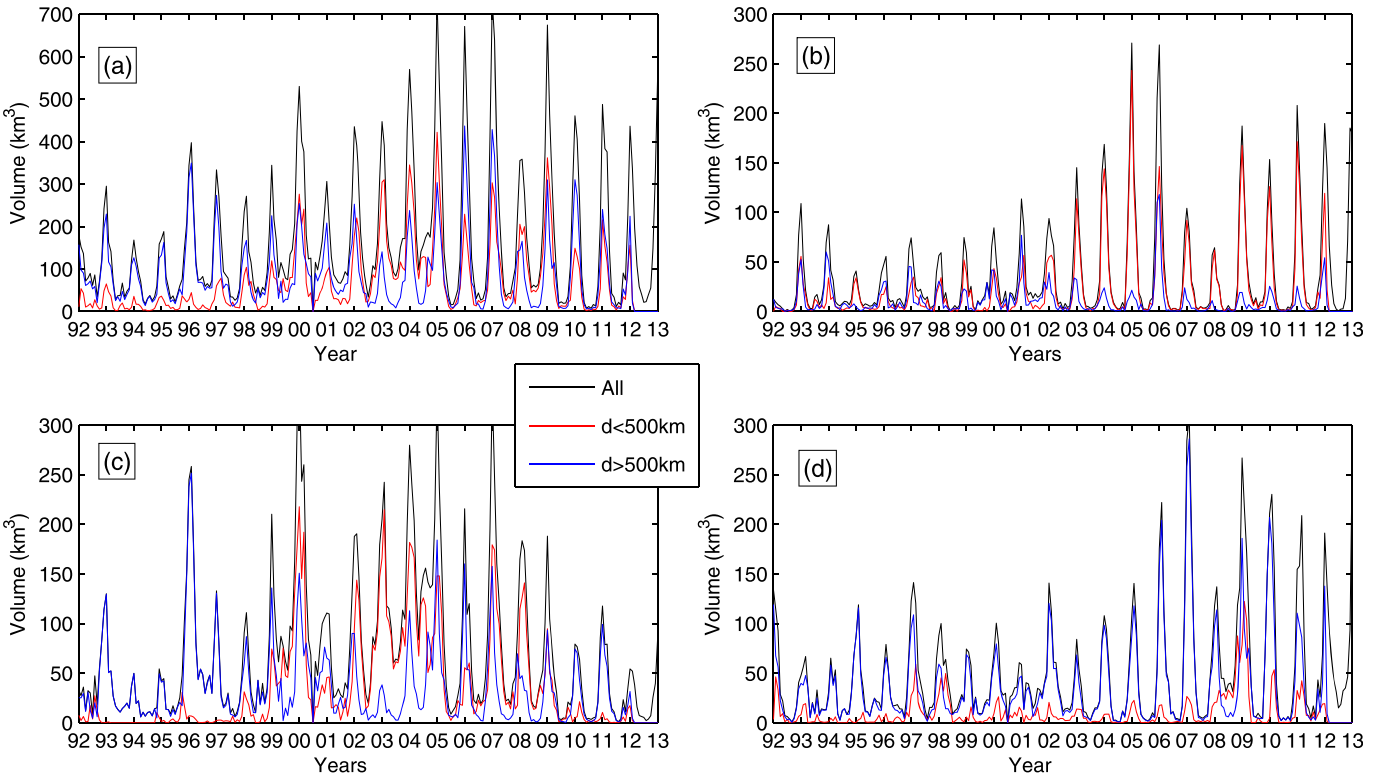

Figure 11. Total volume of ice in open sea (black lines), volume of ice in open sea for icebergs distant by less than 500 km from a large one (red lines) and by more than 500 km (blue lines) for the (a) Southern, (b) South Atlantic, (c) South Indian, and (d) South Pacific Oceans.

overall correlation of 0.66 is large enough to confirm that a large proportion of small icebergs originate from large ones. However, in SA, where vast zones contain only free drifting icebergs, the correlation is almost nil showing that no simple direct relation exists between the volumes of small and large icebergs. In SI and SP, the correlation is medium at about 0.5. This analysis shows that the main general mechanism of generation of small icebergs detected in open water is the fragmentation of large ones. However, small icebergs can drift over long time and distances and can be trapped within sea ice and their paths can significantly differ from those of large icebergs, which strongly conditions their distribution and limits the direct correlation between the volumes of ice.

Cross-correlation analysis allows to measure the similarity of two time series as a function of time lags between them. Three cases are considered, all icebergs and "close" and "free drifting" ones (see figure 13). To mitigate the effect of the strong apparent seasonal cycle, anomalies are considered. For the whole ocean, correlation reaches its maximum of 0.6 for close icebergs at a 3–4 month lag. The generation of small icebergs by fragmentation of large ones takes thus several months to attain its maximum efficiency. For free drifting icebergs, maximum correlation is only 0.4 and is observed at a 12 month lag indicating that at least part of these icebergs results from large ones breaking that are then trapped within sea ice and later released. The cross-correlation analysis in the different basins reveals again very different situations. In SA, correlations are low and always below 0.5. Within this basin, large and small icebergs travel along similar paths especially within the "iceberg alley" while "free drifting" ones are present in vast zones and the analysis shows no clear correlation between the large and small icebergs volumes. SI is mainly characterized by the westward drift of large and small icebergs within the Antarctic Coastal Current, which translates into an absence of correlation for close icebergs. The large correlation observed at lag 0 for free icebergs is quite coincidental and decreases rapidly with time. In SP, the maximum correlation of 0.55 found for close icebergs at a 5 month lag correspond to the breaking of C19A and B15A icebergs that generated large plumes of small icebergs. The correlation for distant icebergs peaks at a medium value 0.47 at a 12 month lag as for the whole ocean. The analysis shows the complexity of the transport of ice. The global volume of ice of close small icebergs is significantly correlated to the large ones volume and the fragmentation process

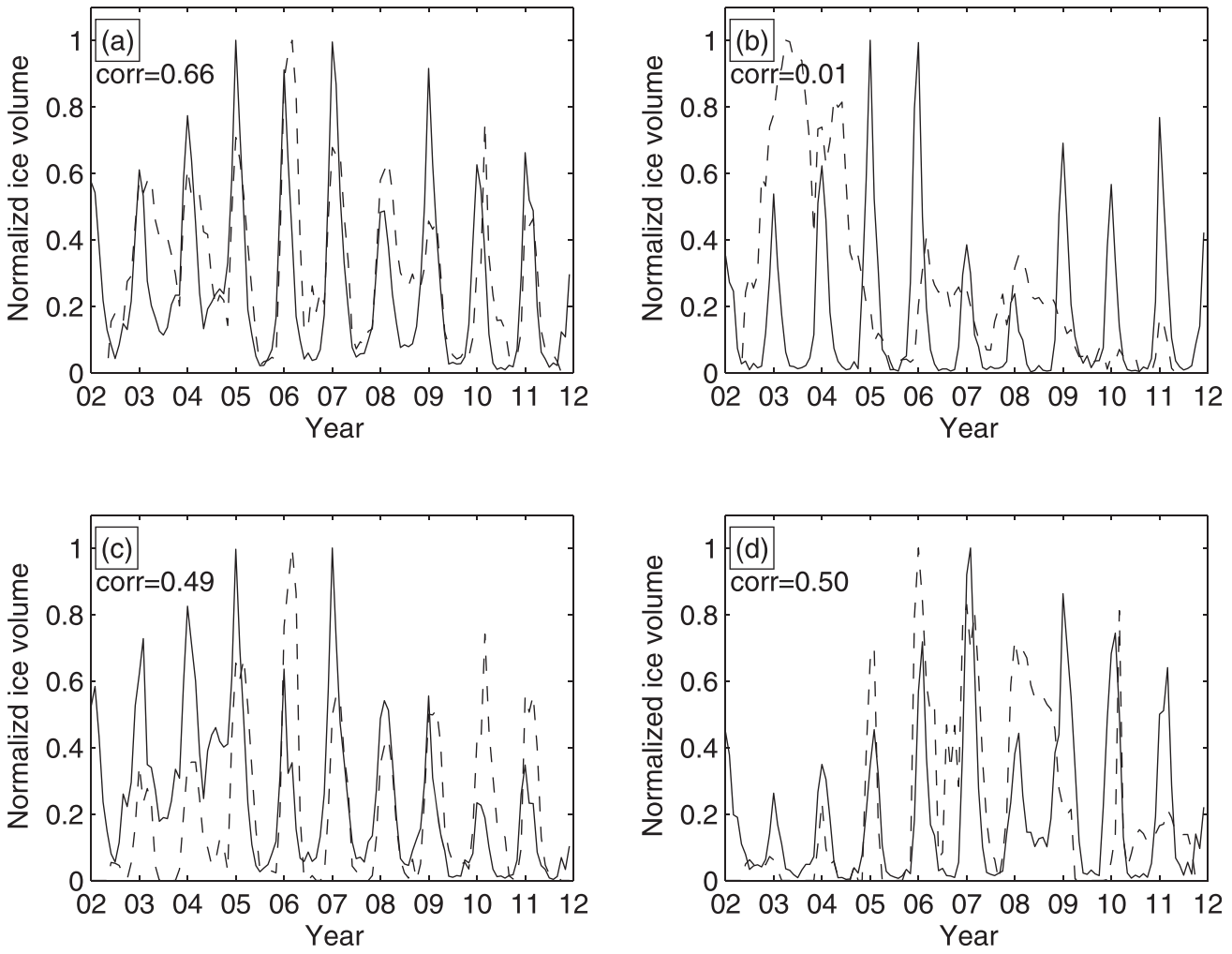

Figure 12. Volume of ice in open sea of small (solid lines) and large (dashed lines) icebergs for (a) the Southern Ocean, (b) the South Atlantic, (c) the Southern Indian, and (d) South Pacific Oceans.

takes several months to be fully efficient. The fragmentation of large icebergs certainly also generates at least part of free drifting icebergs. The time lag indicates that these icebergs are trapped in sea ice for several months. However, large and small icebergs can drift over long times and distances and they can follows very different paths. Because of these differences of trajectories, different volumes of small and large icebergs are transferred from one basin to another resulting in a decorrelation of the two volumes.

The main patterns of the transfer of ice between large and small icebergs are analyzed using the cross correlations between the large and small iceberg monthly volume anomalies. The details of the computation are given in the supporting information. For each grid point, the cross correlation between the large iceberg volume anomaly time series and the small icebergs monthly volume anomalies for all the grid points within a neighborhood of $\pm$2000 km in longitude and $\pm$500 km is computed. For each grid point, the maximum of correlation is determined as well as the associated time lag and small iceberg grid point. Only point with correlation higher than 0.55 is kept in the analysis. To avoid problems due to the lack of data when sea ice is present, only the grid points for which there is less than 6 month of sea ice are considered. This analysis is done for both close and free drifting icebergs. The maximum correlation, time lag, and distance between the large and small grid points are given in supporting information Figure S6. Figure 14 shows the main ice transfer patterns from large icebergs both close and free ones.

The close iceberg analysis clearly reveals the direct generation of small icebergs along well identified trajectories of large ones traveling north. This is especially clear in SI and SP north of 60°S and within the iceberg

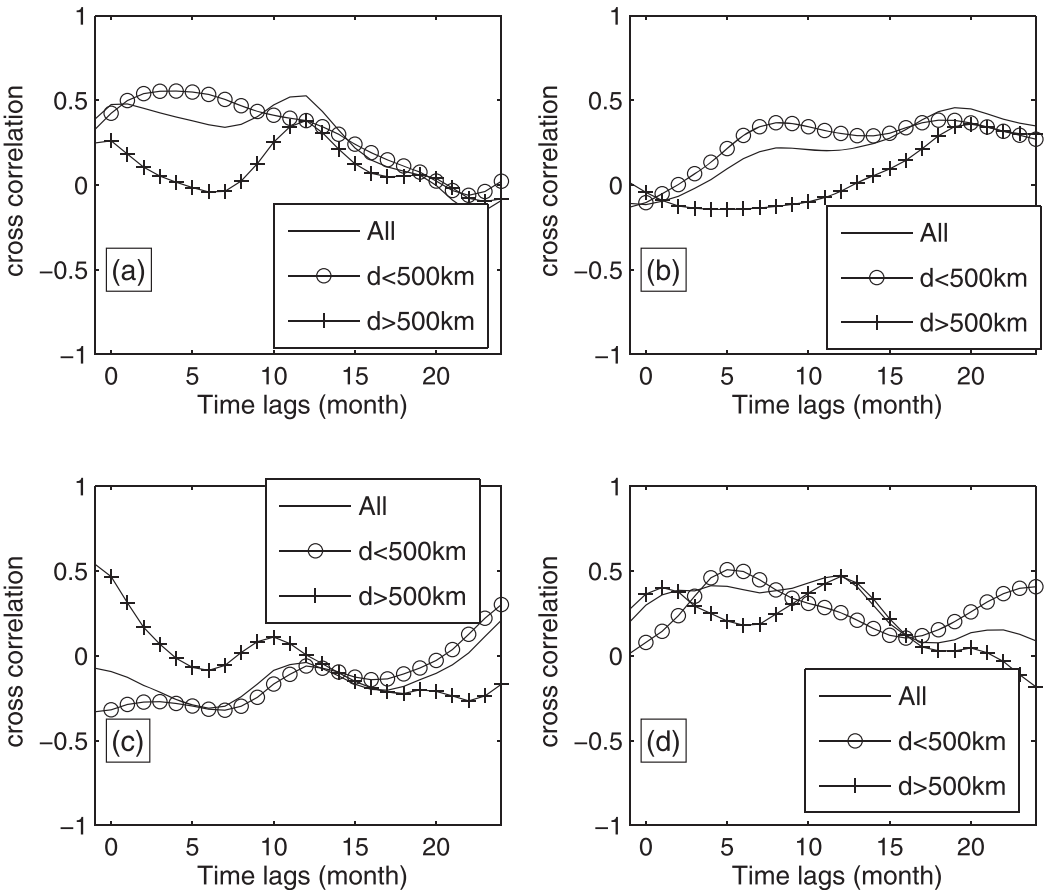

Figure 13. Cross correlation between the large and small icebergs ice volume in open sea for all icebergs (solid lines), icebergs distant by less than 500 km for a large one (circles) and by more than 500 km (crosses) for (a) the Southern Ocean, (b) the South Atlantic, (c) the Southern Indian, and (d) South Pacific Oceans.

alley. These small icebergs that break off large ones diffuse ice for several months (1–6) over several hundreds of kilometers along the large ones trajectories. As melting of small icebergs is more efficient than that of large ones because of their much larger ratio of surface of contact with sea water and volume, the freshwater flux will strongly depends on the small icebergs distribution. This result clearly shows that large icebergs transport ice over large distance and generate plume of smaller bergs that will condition the pattern of the freshwater flux.

It should be noted that the generation of small icebergs near ice shelves is clearly visible along Eastern Antarctica between 0° and 60°E, high correlations are locally observed near emissary regions such as the Prince Harald shelves (34°E).

The cross-correlation analysis of the free drifting icebergs confirms that a significant part of free drifting icebergs results of the breaking of large ones and drift over thousands of kilometers for 6–14 months. For example, several icebergs (B10A, A22B, A38B, and B17A) ground near South Georgia Island (37°W, 54°S) and generate large plumes of small icebergs drifting eastward up to 10°E. In SP, small icebergs that broke off C19A drifted for 14 month over more than 1500 km in the Amundsen and Bellinghausen Seas. This analysis clearly shows the importance of a good representation of the long range transport of ice for ocean circulation modeling.

7. Discussions

The icebergs detection method of *Tournadre et al.* [2012] is used to process the archives of nine altimeters to create a small icebergs data base that spans more than 23 years and to calculate the monthly volume of

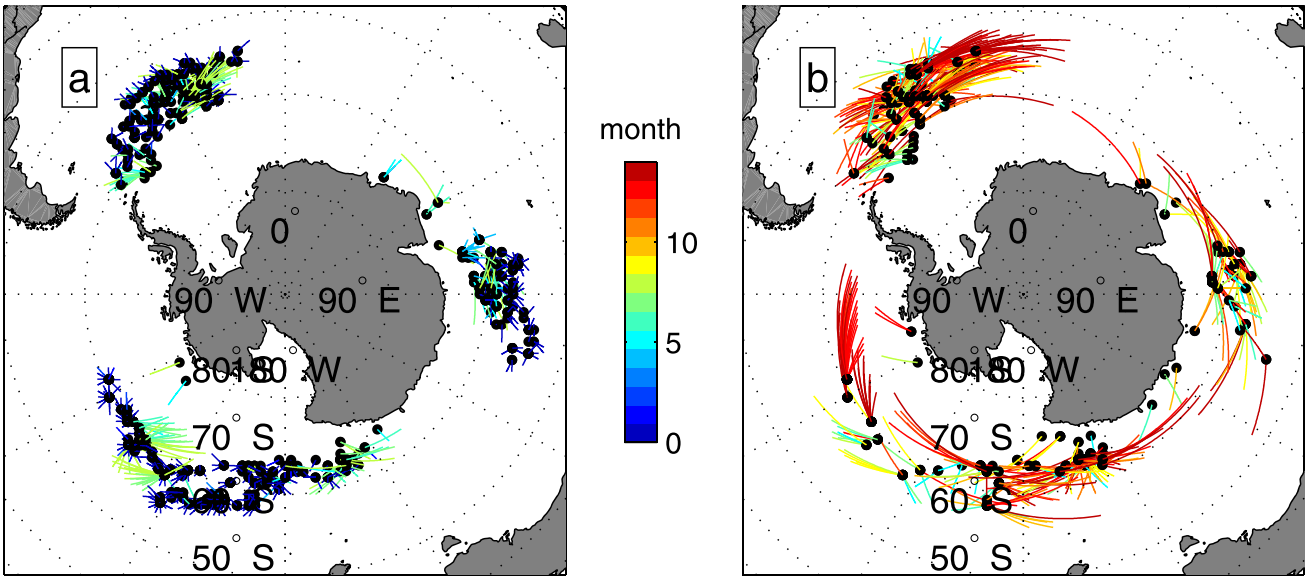

Figure 14. Cross-correlation patterns between the large and small icebergs ice volumes for icebergs distant by (a) less or (b) more than 500 km from a large one. Only points with correlation larger than 0.55 are considered. The lines link the large iceberg (marked by black stars) to the small iceberg grid cell with the highest correlation. The color indicates the time lag.

ice over a regular polar grid. The strong coherence between the different altimeters estimates of icebergs size as well as an intercalibration of volumes allows to estimate a merged homogeneous monthly climatology of small icebergs volume from 1992 to 2014.

The small iceberg (<8 km^2) size distribution and the one for large icebergs (>200 km^2) computed using the *Tournadre et al.* [2015] large iceberg data base follow well power laws of similar slope and can be combined to estimate a general size distribution. This unified distribution follows a power law of slope -1.52 ± 0.32 representative of brittle fragmentation [*Astrom*, 2006; *Spahn et al.*, 2014]. Using this distribution and assuming in a crude approximation that all icebergs have the same thickness, small icebergs (0.1–10 km^2) represent about 3–4% of the total volume while icebergs larger than 100 km^2 make up 89%. The volume of icebergs larger than about 200 km^2 has been shown by *Tournadre et al.* [2015] to decrease from 20,000 km^3 in 2002 to about 10,000 km^3 in 2012. The volume of small icebergs should therefore be of the order of 400–900 km^3 during this period. These values are in very good agreement with the total summer maximum of small icebergs volume estimated by altimeters. About 7–8% (800–1500 km^3) of the total volume should be transported by 10–100 km^2 icebergs whose distribution and melting and breaking are still largely unknown because of lack of data. Sentinel-1a 20 $\times$ 20 km wave mode SAR images acquired every 100 km along track could be a very good candidate to detect and study icebergs of that size and further improve the size and volume distribution.

The general patterns of the small icebergs distribution reflect the general circulation of the Southern Ocean with maximums within the three important gyres, the Kerguelen, Ross, and Weddell gyres [*Orsi et al.*, 1995; *Jacobs et al.*, 2002].

As altimeters can only detect icebergs in open water, the monthly volume of small iceberg presents a strong apparent seasonal cycle that only reflects the surface of the detection area. However, the analysis of the correlation between sea ice extent and volume of ice clearly shows that there is no correlation between the two variables. The interannual variability of volume is thus independent of the sea ice extent one. The volume presents a strong interannual variability that is not in phase in the different ocean basins. This variability is only partially explained by the number of large icebergs present mainly because small icebergs can travel over very long distance and time losing their direct connection with large ones. Vast regions of the ocean, free of large icebergs, are largely populated by small ones showing their importance to estimate the freshwater flux.

Small icebergs can calve directly from Antarctic ice shelves or glaciers. However, the calving flux of icebergs smaller than 8 km^2 can be estimates to be of the order of 112.5 Gt yr^{-1} (using the *Rignot et al.* [2013] and *Depoorter et al.* [2013] calving flux estimates and *Tournadre et al.* [2015] calving flux of icebergs larger than

200 km^2). This flux is significantly smaller than the summer small iceberg volume maximum (200–700 Gt) estimated by altimeters. Fragmentation of large icebergs is a major mechanism of generation of small icebergs.

The overall correlation of 0.66 between the volumes of large and small icebergs within the Southern Ocean confirms this generation process. However, the differential drift of large and small icebergs can strongly limits the correlation at basin scale. The analysis of the cross correlation as a function of the distance between contemporary small and large icebergs shows that the maximum of correlation is reached for close (<500 km) icebergs after a 3–4 month time lags, time for fragmentation to reach its maximum. For more distant small icebergs, the correlation is lower and reaches its maximum of 0.4 after 12 month showing that small icebergs can drift for long periods after having been trapped within sea ice.

The patterns of the transfer of ice from large to small icebergs have been studied by analyzing the cross-correlation patterns between large and small iceberg volumes. For icebergs close to large ones, fragmentation clearly acts as a diffuse process dispersing ice for some months over some hundreds of kilometers along large icebergs trajectories. Depending on the environmental conditions (sea temperature, current, and sea ice), small icebergs generated by fragmentation can drift for long times over thousands of kilometers losing their direct connection to their parents. However, the small and large volumes correlation for these free drifting icebergs is still significant (>0.6) over vast regions of the ocean (especially in SA). North of 65°S the cross-correlation patterns follows quite well the general Southern Ocean circulations patterns with an eastward transport of ice. This analysis shows that, over vast regions, the freshwater flux results from the melting of small icebergs originating from the breaking of large icebergs that have carried ice over thousands of kilometers and sometimes years away from their calving zones. It also shows that a sound modeling of the freshwater flux in the Southern Ocean should take into account the whole variety of processes accounting for ice transport: large-scale transport by large icebergs, fragmentation, drift of smaller icebergs, and final melting.

Further studies can be conducted using the Altiberg database such as the relationship between El Niño Southern Oscillation or Southern Annular Mode and the distribution of icebergs or the interaction between sea ice and icebergs.

Appendix A: Detection Method

The appendix summarized the detection method presented by *Tournadre et al.* [2008, 2012]. An altimeter is a nadir looking radar that emits short pulses that are backscattered by the sea surface. The altimeter measures the backscattered power as a function of time to construct the echo waveform from which the geophysical parameters are estimated [*Chelton et al.*, 2001]. The backscatter coefficient of the waveform can be expressed as a double convolution product of the radar point target response, the flat sea surface response, and the joint probability density function of slope and elevation of the sea surface [*Brown*, 1977]. The backscatter as a function of time, $\sigma(t)$, assuming a Gaussian altimeter pulse, a Gaussian antenna pattern and a Gaussian random distribution of rough-surface specular points, can be expressed as [*Barrick and Lipa*, 1985]

$$\sigma(t)=\frac{1}{2}(2\pi)^{3/2}H''\sigma_\tau\sigma_0\left(1+\mathrm{erf}\left(\frac{x}{\sqrt{2}\sigma_p}\right)\right)e^{-\frac{x}{u_b}} \tag{A1}$$

where $x=ct/2$, $H''=H/(1+H/a)$ is the reduced satellite height, a being the earth's radius, and H the satellite height. σ_τ is the standard deviation of the altimeter pulse; $\sigma_p=\sqrt{h^2+\sigma_\tau^2}$ where h is the RMS wave height; u_b is the antenna pattern standard deviation; and σ_0 is the target backscatter coefficient. The mean sea surface corresponds to $t=0$. The measured waveforms are given in telemetry samples whose width is equal to the length of the pulse and the nominal track point (i.e., the sea level or $t=0$) is shifted to the nominal track point.

A point target of height δ above sea level located at distance d from the satellite nadir will give an echo at the time t_0, or range, defined by [*Powell et al.*, 1993]

$$\frac{ct_0}{2}=-\delta+\frac{1}{2}\frac{a+H}{aH}d^2=-\delta+\frac{d^2}{2H} \tag{A2}$$

The target's range depends only on the orbit parameters and on the target height and distance from nadir. When the satellite flies over the target, the distance from nadir is given by

$$d=\sqrt{d_0^2+(V_{orb}(T-T_0))^2} \tag{A3}$$

where d_0 is the minimum distance at time T_0 between the target and the altimeter ground track, V_{orb} is the satellite ground velocity, and T is the along-track time. The range is thus

$$\frac{ct_0}{2}=-\delta+\frac{d_0^2+V_{orb}^2(T-T_0)^2}{2H''}=-\delta+\frac{d_0^2}{2H''}+\frac{V_{orb}^2}{2H''}(T-T_0)^2 \tag{A4}$$

It is thus a parabola as a function of T. For a given altimeter, all parabolas have the same focal and thus the same shape.

The echo waveform of a point target can be computed using the radar equation [*Roca et al*., 2003]. It is of the form

$$\sigma_{target}(t)=\frac{\sigma_1}{2\pi^2H^4\left(1+\frac{d^2}{2H^2}\right)}e^{-\frac{u_0}{u_b}}e^{-\frac{(x+\delta-u_0)^2}{2\sigma_\tau^2}} \tag{A5}$$

where σ_1 is the target radar cross section, and $u_0=\frac{d^2}{2H''}$.

For an iceberg of area A and constant surface backscatter coefficient σ_1, the waveform is obtained by summation of (A5) over A

$$\sigma_{ice}(t)=\frac{\sigma_1}{2\pi^2H^4}\oint_A\frac{1}{1+\frac{d^2}{2H^2}}e^{-\frac{u_0}{u_b}}e^{-\frac{(x+\delta-u_0)^2}{2\sigma_\tau^2}}dA \tag{A6}$$

An iceberg can be detected if its echo time, t_0 (or range) lies within the altimeter analysis window and a backscatter coefficient is large enough to come out of the thermal noise of the sensor.

The signatures of icebergs in the waveform space (range, along-track coordinate) are parabolas whose shape is defined by (A2). The automated detection is based on the analysis of the convolution product C between a filter F characteristic of an iceberg parabolic signature, and the thermal noise sections of the waveforms.

$$C(i,j)=\sum_{n=n_1}^{n_2}\sum_{m=1}^{M_2}\sigma_0(i,j)F(i-n,j-m) \tag{A7}$$

where i is the telemetry sample index, n_1 and n_2 the range of noise bins used, j, the along-track waveform index, and $\sigma_0(i,j)$, the jth waveform. The filter used has been computed by the waveform model of (A6) for a 100×100 m^2 iceberg. For each waveform, the maximum correlation $C(j)$ and its range $i_{\max}^C(j)$, the maximum backscatter $\sigma_{max}(j)$, and its range $i_{\max}^\sigma(j)$ are determined. A waveform contains an iceberg signature if $C_{max}(j)$ and $\sigma_{max}(j)$ are larger than given thresholds C_1 and σ_1. For each signature, a maximum of 40 waveforms can be involved [*Tournadre et al*., 2008]. If n consecutive waveforms are detected as containing a signature, the range of the echo, t_{ech}, is estimated as

$$t_{ech}=(t_{track}-\min(i_{\max}^\sigma(j),\ j=1..n)) \tag{A8}$$

and the iceberg backscatter, σ_{iceb}, is estimated as the maximum observed backscatter over the whole signature, i.e.,

$$\sigma_{iceb}=\max(\sigma_{\max}(j),\ j=1..n) \tag{A9}$$

Appendix B: Iceberg Area

The range depends on the distance d from nadir of the iceberg center and on the iceberg's free-board elevation h while the iceberg's backscatter depends on the area, A, the distance from nadir d, the backscattering coefficient of the iceberg surface, σ_0^{ice}, which is conditioned by the ice characteristics, the shape and roughness of the iceberg surface, and the presence of snow or water on the iceberg surface. t_{ech} and σ_{iceb} are function of four main unknowns, d, A, h, and σ_0^{ice}. The iceberg area can be estimated if assumptions are made on the values of two of the remaining unknowns (d, h,σ_0^{ice}). σ_0^{ice} is assumed to be constant for all icebergs and set at 19 dB [*Tournadre et al*., 2012]. Following *Gladstone et al*. [2001] and *Romanov et al*. [2012], the free-board elevation for icebergs larger than 200 m is set at 28 m corresponding to a

mean iceberg thickness of 250 m. Using these assumptions, the signature of square icebergs as a function of distance from nadir (0–12 km), and area (0.01–9 km^2) for each altimeter is computed using the analytical model A6. The range $t_{ech} = f(d,A)$ and the mean backscatter $\sigma_{iceb}=g(d,A)$ are estimated from the modeled waveforms and used to compute an inverse model $A=I(t_{ech},\sigma_{iceb})$ and $d=m(t_{ech},\sigma_{iceb})$ for each altimeter.

Appendix C: Volume of Ice

The monthly probability of presence $P(i,j,t)$ (t being the month), over a regular polar stereographic or latitude-longitude grid (i, j) and the mean monthly iceberg area, is computed for each altimeter. $P(i,j,t)$ is simply the ratio of the number N of icebergs detected within a grid cell by the number N_s of valid altimeter samples within the same grid cell

$$P(i,j)=N(i,j)/N_s(i,j) \tag{C1}$$

and $A(i,j,t)$ is defined as [*Tournadre et al.*, 2008]

$$A(i,j,t)=\frac{1}{N(i,j,t)}\sum_{k=1}^{N(i,j,t)} a_k$$

where a_k are the areas of the icebergs detected within the grid cell (i,j) during month t. The total area of the icebergs detected within a grid cell (i,j) is simply

$$S(i,j,t)=\sum_{k=1}^{N(i,j,t)} a_k$$

and as the iceberg thickness H_T is assumed constant, the detected volume of ice is $S(i,j,t)H_T$.

The detected volume of ice per unit area of grid cell is the ratio of the detected volume of ice to the total area sampled by the altimeter over month t, i.e., $S(i,j,t)H_T/(A_{SW}N_s(i,j,t))$ where A_{SW} is the area of an altimeter effective swath. Assuming that the monthly iceberg distribution within a grid cell is uniform, the total volume of ice within the grid cell is the product of the volume per unit area by the area of the grid cell, i.e.,

$$V(i,j,t)=\frac{S(i,j,t)H_T}{A_{SW}N_s(i,j,t)}\Delta x_i \Delta y_j \tag{C2}$$

The altimeter swath for 28 m free-board icebergs A_{SW} is the product of the altimeter along-track resolution by the range of distance from nadir over which an iceberg can be detected. Using A2, the range of detection of an iceberg is given by

$$\sqrt{(ct_0+2h)H''}+\frac{\bar{d}_0}{2} \geq d \geq \sqrt{(ct_1+2h)H''}-\frac{\bar{d}_0}{2} \tag{C3}$$

thus,

$$A_{SW}=2(\sqrt{(ct_o+2h)H''}-\sqrt{(ct_1+h)H''}+d_0) \tag{C4}$$

where d_0 is the mean iceberg length, and t_0 and t_1 are the time limits of the usable noise range part of the waveform. The factor 2 accounts for the left-right ambiguity of detection.

Appendix D: Distribution of Iceberg Size

Two models of distributions have been considered for the size distributions. The two-parameter lognormal distribution f_X is defined by

$$f_X(x;\mu,\sigma)=\frac{1}{x\sigma\sqrt{2\pi}}e^{-\frac{(\ln x-\mu)^2}{2\sigma^2}},\ x>0 \tag{D1}$$

where μ and σ are the location and scale parameters, respectively. The mean of the distribution is then defined by $e^{\mu+\frac{\sigma^2}{2}}$.

The power law distribution f_X is defined by

$$f_X(x;\alpha) = Cx^{-\alpha},\ x > x_{\min} \tag{D2}$$

with $C = \frac{\alpha-1}{x_{\min}} x_{\min}^{\alpha-1}$.

It should be noted that if the σ parameter is large enough the logarithm of the lognormal density function appears linear for a large range of value and can be approximated by a power law.

Acknowledgments

The ERS-1, ERS-2, Envisat, and Cryosat altimeter data were provided by the European Space Agency. The Jason-1, Jason-2, and SARAL/AltiKa data were made available by the AVISO center, while the Topex data were provided by NASA Jet Propulsion Laboratory. The HY2A data were provides by the Chinese National Satellite Ocean Application Service (NSOAS). The study was partially funded by the Centre National d'Etudes Spatiales under the TOSCA program. The authors would like to thank the anonymous reviewers whose comments greatly help to improve the article.

References

Astrom, J. A. (2006), Statistical models of brittle fragmentation, *Adv. Phys.*, *55*(3–4), 247–278, doi:10.1080/00018730600731907.

Barrick, D., and B. Lipa (1985), Analysis and interpretation of altimeter sea echo, *Satell. Oceanic Remote Sens. Adv. Geophys.*, *27*, 61–100.

Brown, G. S. (1977), The average impulse response of a rough surface and its applications, *IEEE Trans. Antennas Propag., AP-25*, 67–74.

Chelton, D. E., J. C. Ries, B. J. Haines, L.-L. Fu, and P. S. C. Callahan (2001), An Introduction to Satellite Altimetry, in *Satellite Altimetry and Earth Science: A Handbook of Techniques and Applications*, chap. I, 463 pp., Academic, San Diego, Calif.

Depoorter, M. A., J. L. Bamber, J. A. Griggs, J. T. M. Lenaerts, S. R. M. Ligtenberg, M. R. van den Broeke, and G. Moholdt (2013), Calving fluxes and basal melt rates of Antarctic ice shelves, *Nature*, *502*, 89–92, doi:10.1038/nature12567.

Gladstone, R. M., G. R. Bigg, and K. W. Nicholls (2001), Iceberg trajectory modeling and meltwater injection in the Southern Ocean, *J. Geophys. Res.*, *106*, 19,903–19,916, doi:10.1029/2000JC000347.

Glasby, G. P. (Ed.) (1990), *Antarctic Sector of the Pacific*, 396 pp., Elsevier, Amsterdam.

Grotov, A. S., D. A. Nechaev, G. G. Panteleev, and M. I. Yaremchuk (1998), Large scale circulation in the Bellingshausen and Amundsen Seas as a variational inverse of climatological data, *J. Geophys. Res.*, *103*(C6), 13,011–13,022, doi:10.1029/98JC00449.

Jacka, T. H., and A. B. Giles (2007), Antarctic iceberg distribution and dissolution from ship-based observations, *J. Glaciol.*, *53*, 341–356.

Jacobs, S. S., H. Hellmer, C. Doake, A. Jenkins, and R. Frolich (1992), Melting of ice shelves and the mass balance of Antarctica, *J. Glaciol.*, *38*(130), 375–387.

Jacobs, S. S., C. F. Giulivi, and P. A. Mele (2002), Freshening of the Ross Sea during the late 20th century, *Science*, *297*(5580), 386–389, doi:10.1126/science.1069574.

Joughin, I., and L. Padman (2003), Melting and freezing beneath Filchner-Ronne Ice Shelf, Antarctica, *Geophys. Res. Lett.*, *30*(9), 1477, doi:10.1029/2003GL016941.

Keys, J., and D. Fowler (1989), Sources and movement of icebergs in the south-west Ross Sea, Antarctica, *Ann. Glaciol.*, *12*, 85–88.

Klatt, O., E. Fahrbach, M. Hoppema, and G. Rohardt (2005), The transport of the Weddell gyre across the prime meridian, *Deep Sea Res., Part II*, *52*(3–4), 513–528, doi:10.1016/j.dsr2.2004.12.015.

Lancelot, C., A. de Montety, H. Goosse, S. Becquevort, V. Schoemann, B. Pasquer, and M. Vancoppenolle (2009), Spatial distribution of the iron supply to phytoplankton in the Southern Ocean: A model study, *Biogeosciences*, *6*, 2861–2878.

Lellouche, J.-M., et al. (2013), Evaluation of global monitoring and forecasting systems at Mercator Océan, *Ocean Sci.*, *9*(1), 57–81, doi:10.5194/os-9-57-2013.

Long, D., J. Ballantyne, and C. Bertoia (2002), Is the number of icebergs really increasing?, *EOS Trans. AGU*, *83*(42), 469–474.

McCartney, M. S., and K. A. Donohue (2007), A deep cyclonic gyre in the Australian-Antarctic basin, *Prog. Oceanogr.*, *75*(4), 675–750.

Orsi, A. H., T. Whitworth III, and W. D. Nowlin Jr. (1995), On the meridional extent and fronts of the Antarctic Circumpolar Current, *Deep Sea Res., Part I*, *42*(5), 641–673, doi:10.1016/0967-0637(95)00021-W.

Powell, R. J., A. R. Birks, W. J. Wrench, and C. L. Biddiscombe (1993), Using transponders with ERS1-1 and Topex altimeters to measure orbit altitude to ±3 cm, in *Proceedings of First ERS-Symposium (ESA SP-359)*, pp. 511–516. Cannes, 1992, ESA Publication Division, Nordwijk.

Queffeulou, P. (2013), Merged altimeter data base, an update, in *Proceedings of ESA Living Planet Symposium*, vol. ESA SP-722, edited by E. Communications, Eur. Space Res. and Technol. Cent., AG Noordwijk, Netherlands.

Raiswell, R., L. G. Benning, M. Tranter, and S. Tulaczyk (2008), Bioavailable iron in the Southern Ocean: The significance of the iceberg conveyor belt, *Geochem. Trans.*, *9*, doi:10.1186/1467-4866-9-7.

Raynal, M. (2014), Hy-2a: Global statistical assessment and cross-calibration with Jason-2 over ocean, *Tech. Rep. SALP-NT-M-EA-22364-CLS, CLS-DOS-NT-14-148*, Collect. Localisation Satell., Ramonville Saint-Agne, France.

Rémy, F., T. Flament, A. Michel, and D. Blumstein (2015), Envisat and SARAL/AltiKa observations of the Antarctic ice sheet: A comparison between the Ku-band and Ka-band, *Mar. Geod.*, *38*, suppl. 1, 510–521, doi:10.1080/01490419.2014.985347.

Riffenburgh, B. (Ed.) (2007), *Encyclopedia of the Antarctic*, 1272 pp., Routledge, N. Y.

Rignot, E., and S. S. Jacobs (2002), Rapid bottom melting widespread near Antarctic ice sheet grounding lines, *Science*, *296*(5575), 2020–2023, doi:10.1126/science.1070942.

Rignot, E., S. Jacobs, J. Mouginot, and B. Scheuchl (2013), Ice-shelf melting around Antarctica, *Science*, *341*, 266–270.

Roca, M., H. Jackson, and C. Celani (2003), RA-2 sigma-0 absolute calibration, in *Proceedings of Envisat Validation Workshop (ESA SP-531)*, 16 pp. Frascati, Italy, 9 – 13 December 2002, ESA Publication Division Nordwijk.

Romanov, Y., N. A. Romanova, and P. Romanov (2012), Shape and size of Antarctic icebergs derived from ship observation data, *Antarct. Sci.*, *24*, 77–87, doi:10.1017/S0954102011000538.

Romanov, Y. A., N. A. Romanova, and P. Romanov (2008), Distribution of icebergs in the Atlantic and Indian ocean sectors of the Antarctic region and its possible links with ENSO, *Geophys. Res. Lett.*, *35*, L02506, doi:10.1029/2007GL031685.

Scharroo, R., W. Smith, J. Lillibridge, and E. Leuliette (2012), Cal/Val of combined conventional and reduced SAR over oceans and in the coastal regime, paper presented at 6th Coastal Altimetry Workshop - 2012. Riva del Garda, Italy, ESA. [Available at http://www.coastalt.eu/files/gardaworkshop12/pres/.]

Schodlok, M. P., H. H. Hellmer, G. Rohardt, and E. Fahrbach (2006), Weddell Sea iceberg drift: Five years of observations, *J. Geophys. Res.*, *111*, C06018, doi:10.1029/2004JC002661.

Silva, T., G. Bigg, and K. Nicholls (2006), The contribution of giant icebergs to the Southern Ocean freshwater flux, *J. Geophys. Res.*, *111*, C03004, doi:10.1029/2004JC002843.

Spahn, F., E. V. Neto, A. H. F. Guimarães, A. N. Gorban, and N. V. Brilliantov (2014), A statistical model of aggregate fragmentation, *New J. Phys.*, *16*(1), 013031.

Stammer, D. (2008), Response of the global ocean to Greenland and Antarctic ice melting, *J. Geophys. Res.*, *113*, C06022, doi:10.1029/2006JC004079.

Stuart, K. M., and D. G. Long (2011), Tracking large tabular icebergs using the SeaWinds Ku-band microwave scatterometer, *Deep Sea Res., Part II*, *58*(11–12), 1285–1300, doi:10.1016/j.dsr2.2010.11.004.

Thibaut, P., and N. Steunou (2013), Sigma0 analysis comparison of MLE3 and MLE4 and with Jason-2 Ku band: Analysis of the attenuation algorithm, paper presented at SARAL/AltiKa NRT Verification Workshop, AVISO, Collect. Localisation Satell., Toulouse. [Available at www.aviso.altimetry.fr.]

Tournadre, J. (2007), Signature of lighthouses, ships, and small islands in altimeter waveforms, *J. Atmos. Oceanic Technol.*, *24*, 1143–1149.

Tournadre, J., K. Whitmer, and F. Girard-Ardhuin (2008), Iceberg detection in open water by altimeter waveform analysis, *J. Geophys. Res.*, *113*, C08040, doi:10.1029/2007JC004587.

Tournadre, J., F. Girard-Ardhuin, and B. Legresy (2012), Antarctic icebergs distributions, 2002–2010, *J. Geophys. Res.*, *117*, C05004, doi:10.1029/2011JC007441.

Tournadre, J., N. Bouhier, F. Girard-Ardhuin, and F. Rémy (2015), Large icebergs characteristics from altimeter waveforms analysis, *J. Geophys. Res.*, *120*, 1954–1974, doi:10.1002/2014JC010502.

Wesche, C., and W. Dierking (2015), Near-coastal Circum-Antarctic iceberg size distributions determined from synthetic aperture radar images, *Remote Sens. Environ.*, *156*, 561–569, doi:10.1016/j.rse.2014.10.025.